
AN ADAPTIVE FINITE DIFFERENCE METHOD FOR TOTAL VARIATION MINIMIZATION

Thomas JACUMIN
LTH, University of Lund, Sweden
thomas.jacumin@math.lth.se

Andreas LANGER
LTH, University of Lund, Sweden
andreas.langer@math.lth.se

October 18, 2024

ABSTRACT

In this paper, we propose an adaptive finite difference scheme in order to numerically solve total variation type problems for image processing tasks. The automatic generation of the grid relies on indicators derived from a local estimation of the primal-dual gap error. This process leads in general to a non-uniform grid for which we introduce an adjusted finite difference method. Further we quantify the impact of the grid refinement on the respective discrete total variation. In particular, it turns out that a finer discretization may lead to a higher value of the discrete total variation for a given function. To compute a numerical solution on non-uniform grids we derive a semi-smooth Newton algorithm in 2D for scalar and vector-valued total variation minimization. We present numerical experiments for image denoising and the estimation of motion in image sequences to demonstrate the applicability of our adaptive scheme.

Keywords Total variation, Non-smooth optimization, Image reconstruction, Optical flow estimation, Adaptive finite difference discretization

Mathematics Subject Classification 49M29, 65K10, 90C47, 94A08

1 Introduction

In [40] total variation (TV) was introduced as a regularization technique to imaging problems. Given the effectiveness of this regularization, in particular thanks to its property of preserving discontinuities in the solution, since then total variation is widely used in image processing. For example, it shows its efficiency for image inpainting [41], image denoising [12, 16], image zooming [14] and optical flow estimation [44], only to mention a few applications where total variation regularization is successfully applied. Thereby the problem typically states as follows: let $\Omega \subset \mathbb{R}^d$ be an open, bounded and simply connected domain with Lipschitz boundary, where $d \in \mathbb{N}$ denotes the spatial dimension, then one solves

$$\inf_{\mathbf{u} \in L^2(\Omega)^m \cap \text{BV}(\Omega)^m} \mathcal{D}(T\mathbf{u}, g) + \lambda \int_{\Omega} |D\mathbf{u}|_{F,r}. \quad (1)$$

Here $m \in \mathbb{N}$ denotes the number of channels, e.g. $m = 1$ for scalar images or $m = d$ for motion fields, $g \in L^2(\Omega)$ is the given data, $T : L^2(\Omega)^m \rightarrow L^2(\Omega)$ is a bounded linear operator, \mathcal{D} is a data fitting term enforcing the consistency between g and the solution, and $\lambda > 0$ is the regularization parameter. Further $\text{BV}(\Omega)^m$ denotes the space of m -vector-valued functions with bounded variation, i.e. $\text{BV}(\Omega)^m := \{\mathbf{u} \in L^1(\Omega)^m \mid \int_{\Omega} |D\mathbf{u}|_{F,r} < +\infty\}$ with $\int_{\Omega} |D\mathbf{u}|_{F,r}$ being the total variation of \mathbf{u} in Ω defined by

$$\int_{\Omega} |D\mathbf{u}|_{F,r} := \sup \left\{ \int_{\Omega} \mathbf{u} \cdot \text{div } \mathbf{v} \mid \mathbf{v} \in (C_0^\infty(\Omega)^d)^m, |\mathbf{v}|_* \leq 1 \text{ for } \mu\text{-almost every } x \in \Omega \right\}.$$

The work was supported by the Crafoord Foundation through the project ‘‘Locally Adaptive Methods for Free Discontinuity Problems’’.

The operator $\text{div} : (C_0^\infty(\Omega)^d)^m \rightarrow C_0^\infty(\Omega)^m$ describes the divergence, $|\cdot|_{F,r} : \mathbb{R}^{d \times m} \rightarrow \mathbb{R}$ denotes the r -Frobenius norm defined as

$$|\mathbf{v}|_{F,r} := \left(\int_{\Omega} \sum_{n=1}^m \sum_{k=1}^d |v_{nk}|^r dx \right)^{1/r}$$

for $\mathbf{v} = ((v_{11}, \dots, v_{1d}), \dots, (v_{m1}, \dots, v_{md})) \in (C_0^\infty(\Omega)^d)^m$ and $r \geq 1$, and $|\cdot|_*$ is the dual norm of the r -Frobenius norm.

In the presence of noise, the choice of the data fitting term \mathcal{D} typically depends on the nature of the noise contamination. Specifically, a quadratic L^2 -norm is used if the data is corrupted by Gaussian noise [15], whereas an L^1 -norm is preferred for data affected by impulse noise [4, 36, 37]. Using these data fitting terms, we refer to (1) as the L^2 -TV model and the L^1 -TV model, respectively. In cases where both Gaussian and impulse noise are present simultaneously in the data, a combined L^1/L^2 data fitting term has been shown to be effective [25, 31, 32]. Then (1) reads as

$$\inf_{\mathbf{u} \in L^2(\Omega)^m \cap \text{BV}(\Omega)^m} \alpha_1 \|T\mathbf{u} - g\|_{L^1(\Omega)} + \frac{\alpha_2}{2} \|T\mathbf{u} - g\|_{L^2(\Omega)}^2 + \lambda \int_{\Omega} |D\mathbf{u}|_{F,r}, \quad (2)$$

where $\alpha_1, \alpha_2 \geq 0$, which we call the L^1 - L^2 -TV model. In this paper we will consider the L^1 - L^2 -TV model due to its generality, since it includes the L^2 -TV model ($\alpha_1 = 0$) and the L^1 -TV model ($\alpha_2 = 0$).

When looking at a concrete digital image, the underlying analog image is usually discretized by square pixels of uniform size. For further image enhancement (e.g. removing noise) or image analysis (e.g. motion estimation), this strongly supplies a finite difference implementation of image processing algorithms. Hence, for finding a numerical solution of (2) this means discretizing (2) by utilizing a finite difference method on a uniform grid. Despite the good quality of the reconstruction, using such a uniform discretization can lead to numerous degrees of freedom and, as a result, to an expensive computational cost, which is particularly problematic for large scale images.

It is worth mentioning that other discretization methods for total variation minimization have been considered, such as the finite element method [17] and a neural network based method [33]. In the finite element framework, adaptive discretization based on a posteriori error estimates has been employed to reduce the degrees of freedom in the problem [7, 26]. The L^1 - L^2 -TV model has also been studied in this context [2, 3, 23]. In particular, in [2] an adaptive finite element coarse-to-fine scheme has been proposed showing a significant speed-up in computational time. Challenges arise when selecting the finite element space. When using the space of piecewise constant functions, Γ -convergence of the finite dimensional problem to the infinite dimensional cannot be expected, as demonstrated by a counterexample in [6]. In contrast, such a convergence result holds when using the space of continuous and piecewise linear functions [29, 33], though this approach prevents the reconstruction from exhibiting discontinuities [3]. Furthermore, using finite differences for images may seem more natural than using finite elements, as the data (i.e. pixels) are organized on a uniform discrete grid.

Adaptive finite difference methods have long been explored in the literature for solving a variety of partial differential equations (PDEs); see, for example, [9, 35] and references therein. More recently, in [39] a finite difference scheme on non-uniform grids within a general framework for solving nonlinear PDEs is introduced. Although this approach is quite flexible, it does not extend to total variation minimization. As such, to the best of our knowledge, no adaptive finite difference method has been proposed for (2).

In this paper, we suggest to solve the L^1 - L^2 -TV model by combining a finite difference method with an adaptive refinement strategy. This allows us on the one hand to reduce the number of degrees of freedom, while on the other hand we do not need to make a choice of a function space. In our refinement process we use a cell-centered sampling, that is the degrees of freedom are in the middle of the elements, allowing us to mimic a piecewise constant function, which is well suited for discontinuity-preserving problems. Further we opted for a coarse-to-fine approach. That is we start with a coarse grid and subsequently subdivide the marked elements into four smaller elements to enhance the accuracy of the reconstruction. The marking of the elements is based on a local error indicator which is derived from a primal-dual gap error estimate following the idea in [8]. We note that the error of the total variation due to a finite difference discretization has been estimated in some works [13, 42]. However, since these estimates are global, they are not suitable for grid adaptivity. For computing a solution on the obtained non-uniform grid we adapt the primal-dual semi-smooth Newton method derived and analyzed in [23] to our finite difference setting.

We theoretically analyze the influence of the grid refinement on a discretized total variation. From considerations in [13, 18] one implies that the discrete total variation of a function can be mesh dependent, although this is not highlighted there. In this paper we make an effort and quantify the impact of a refinement on the discrete total variation. In fact we derive a pixel-wise constant function that is bounded above by one, indicating that a refinement either keeps or increases the total variation of a function.

The article is organized as follows: in Section 2, we introduce the primal-dual setting of the considered problem before we address in Section 3 its discretization on non-uniform grids. Section 4 is devoted to the derivation of adaptive finite difference schemes. The impact of mesh refinement on the total variation is analyzed and quantified in Section 5. Section 6 focuses on computing the primal-dual gap error and proposes a local indicator essential for mesh adaptivity. In Section 7, we present a semi-smooth Newton algorithm to effectively solve the L^1 - L^2 -TV problem, followed by numerical experiments in Section 8 to validate our approach.

2 Formulation of the Model

For a Hilbert space H we denote by $\langle \cdot, \cdot \rangle_H$ its inner product and by $\| \cdot \|_H$ its induced norm. The duality pairing between H and its continuous dual space H^* is written as $\langle \cdot, \cdot \rangle_{H, H^*}$. For functions $\mathbf{v} = (v_1, \dots, v_m)$, $\mathbf{w} = (w_1, \dots, w_m) \in L^2(\Omega)^m$ we define

$$\langle \mathbf{v}, \mathbf{w} \rangle_{L^2(\Omega)^m} := \sum_{k=1}^m \langle v_k, w_k \rangle_{L^2(\Omega), L^2(\Omega)} \quad \text{and} \quad \|\mathbf{v}\|_{L^2(\Omega)^m}^2 := \langle \mathbf{v}, \mathbf{v} \rangle_{L^2(\Omega)^m},$$

and for $\mathbf{v} = (\mathbf{v}_1, \dots, \mathbf{v}_m)$, $\mathbf{w} = (\mathbf{w}_1, \dots, \mathbf{w}_m) \in (L^2(\Omega)^d)^m$ we write

$$\langle \mathbf{v}, \mathbf{w} \rangle_{(L^2(\Omega)^d)^m} := \sum_{k=1}^m \langle \mathbf{v}_k, \mathbf{w}_k \rangle_{L^2(\Omega)^d} \quad \text{and} \quad \|\mathbf{v}\|_{(L^2(\Omega)^d)^m}^2 := \langle \mathbf{v}, \mathbf{v} \rangle_{(L^2(\Omega)^d)^m}.$$

For a bounded and linear operator Λ between two Banach spaces we denote by Λ^* its adjoint operator.

As in [23], we consider the following penalized version of (2)

$$\inf_{\mathbf{u} \in H^1(\Omega)^m} \left\{ E(\mathbf{u}) := \alpha_1 \|T\mathbf{u} - g\|_{L^1(\Omega)} + \frac{\alpha_2}{2} \|T\mathbf{u} - g\|_{L^2(\Omega)}^2 + \frac{\beta}{2} \|S\mathbf{u}\|_{V_S}^2 + \lambda \int_{\Omega} |\nabla \mathbf{u}|_{F,r} dx \right\}, \quad (\mathcal{P})$$

where $S : H^1(\Omega)^m \rightarrow V_S$ is a bounded linear operator for some Hilbert space V_S and $\beta \geq 0$ typically chosen very small such that \mathcal{P} is a close approximation of (2). A primal-dual framework for (\mathcal{P}) has been developed in [23] for the following settings of S and its related space V_S :

- $S = Id$, then $V_S \subseteq L^2(\Omega)^m$ and $\| \cdot \|_{V_S} = \| \cdot \|_{L^2(\Omega)^m}$,
- $S = \nabla$, then $V_S \subseteq (L^2(\Omega)^d)^m$ and $\| \cdot \|_{V_S} = \| \cdot \|_{(L^2(\Omega)^d)^m}$.

We suppose that $B := \alpha_2 T^* T + \beta S^* S$ is invertible, which is, for example, the case for $\beta > 0$ and $S = I$, even if T is not injective. Further, we define $\| \cdot \|_{B^{-1}}^2 := \langle \cdot, B^{-1} \cdot \rangle_{L^2(\Omega)^m}$. The dual problem of (\mathcal{P}) reads

$$\sup_{(p_1, \mathbf{p}_2) \in L^2(\Omega) \times (L^2(\Omega)^d)^m} \left\{ D(p_1, \mathbf{p}_2) := -\frac{1}{2} \|T^* p_1 + \nabla^* \mathbf{p}_2 - \alpha_2 T^* g\|_{B^{-1}}^2 + \frac{\alpha_2}{2} \|g\|_{L^2(\Omega)}^2 - \langle g, p_1 \rangle_{L^2(\Omega)} \right. \\ \left. - \chi_{|p_1| \leq \alpha_1} - \chi_{|\mathbf{p}_2|_{F,s} \leq \lambda} \right\}, \quad (\mathcal{D})$$

cf. [23], where $r^{-1} + s^{-1} = 1$. The function χ is defined for a given predicate $\omega : \Omega \rightarrow \{\text{true}, \text{false}\}$ by

$$\chi_{\omega}(x) := \begin{cases} 0, & \text{if } \omega(x) \text{ is true,} \\ +\infty, & \text{otherwise,} \end{cases}$$

for $x \in \Omega$.

3 Problem Discretization on Non-Uniform Grid

In this section, we introduce a finite difference discretization of (\mathcal{P}) , focusing on the two-dimensional case ($d = 2$), despite an extension to other dimensions seems possible. This discretization triangulates the domain Ω by a family of squares $(E_i)_{i=1}^N$, $N \in \mathbb{N}$ denoting the degrees of freedom, where element E_i has side length h_i and center $\mathbf{x}_i \in \Omega$. In addition, we define the discrete domain Ω_h as the collection of centers, i.e. $\Omega_h := \{\mathbf{x}_i \in \Omega \mid i = 1, \dots, N\}$.

The mesh is implemented using a *quad-tree* data structure [19]. A quad-tree is a tree-shaped structure where each non-leaf node has four branches. Each node in the quad-tree represents a square. If a node has branches, then its

branches represent the four smaller squares that make up the larger square represented by the node. We *refine* an element by dividing it into four sub-elements, which involves adding four child nodes to its corresponding leaf node. To ensure specific mesh patterns and simplify the derivation of the finite difference scheme, we impose the following constraint: each element of the mesh must either be the same length as its neighboring elements or be twice or half as large. We refer to Figure 1 for an example of such a mesh. A function v mapping from Ω to \mathbb{R} is discretized by a vector

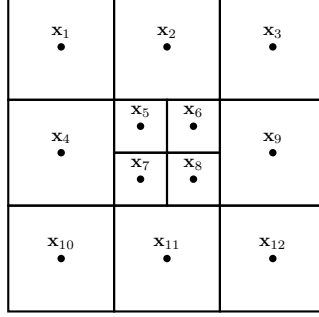


Figure 1: Example of an adaptive grid.

$v_h \in \mathbb{R}^N$ where each component $(v_h)_i$ is defined as $h_i^{-2} \int_{E_i} v dx$, for $i = 1, \dots, N$. The following scalar product and norm are then used for $v_h, w_h \in \mathbb{R}^N$

$$\langle v_h, w_h \rangle_{L^2(\Omega_h)} := \sum_{i=1}^N h_i^2 (v_h)_i (w_h)_i, \quad \text{and} \quad \|v_h\|_{L^2(\Omega_h)}^2 := \langle v_h, v_h \rangle_{L^2(\Omega_h)}.$$

Note that the definition above is the exact numerical integration for a piecewise constant function, in particular $\langle v_h, w_h \rangle_{L^2(\Omega_h)} = \langle I_h v_h, I_h w_h \rangle_{L^2(\Omega)}$, where I_h is the piecewise constant interpolation. Moreover, $I_h g_h$ is the L^2 -projection of g into the space of piecewise constant functions. The main motivation for such a choice of interpolation is that, since a digital image is a set of pixels, the discontinuities are located between the pixels. As a consequence, using a linear interpolation would lead to a smoothing of the discontinuities, which we want to avoid, cf. [3, Figure 2] in a finite element setting. We discretize a function $\mathbf{v} = (v_1, \dots, v_m)$ from Ω to \mathbb{R}^m by a vector $\mathbf{v}_h \in \mathbb{R}^{mN}$ such that $(\mathbf{v}_h)_{(k-1)N+i} := v_k(\mathbf{x}_i)$, for $i = 1, \dots, N$ and $k = 1, \dots, m$. We use the following scalar product and norm for $\mathbf{v}_h, \mathbf{w}_h \in \mathbb{R}^{mN}$

$$\langle \mathbf{v}_h, \mathbf{w}_h \rangle_{L^2(\Omega_h)^m} := \sum_{i=1}^N h_i^2 \sum_{k=1}^m (\mathbf{v}_h)_{(k-1)N+i} (\mathbf{w}_h)_{(k-1)N+i} \quad \text{and} \quad \|\mathbf{v}_h\|_{L^2(\Omega_h)^m}^2 := \langle \mathbf{v}_h, \mathbf{v}_h \rangle_{L^2(\Omega_h)^m}.$$

A gradient-like function $\mathbf{w} = ((w_{11}, w_{12}), \dots, (w_{m1}, w_{m2}))$ from Ω to $(\mathbb{R}^2)^m$ is discretized by a vector $\mathbf{w}_h \in \mathbb{R}^{2mN}$ such that $(\mathbf{w}_h)_{2(n-1)N+(k-1)N+i} := w_{kn}(\mathbf{x}_i)$, for $n = 1, \dots, m$ and $k = 1, 2$. For $\mathbf{w}_h, \mathbf{q}_h \in \mathbb{R}^{2mN}$, we introduce the scalar product

$$\langle \mathbf{w}_h, \mathbf{q}_h \rangle_{(L^2(\Omega_h)^2)^m} := \sum_{i=1}^N h_i^2 \sum_{n=1}^m \sum_{k=1}^2 (\mathbf{w}_h)_{2(n-1)N+(k-1)N+i} (\mathbf{q}_h)_{2(n-1)N+(k-1)N+i},$$

and the norm

$$\|\mathbf{w}_h\|_{(L^2(\Omega_h)^2)^m}^2 := \langle \mathbf{w}_h, \mathbf{w}_h \rangle_{(L^2(\Omega_h)^2)^m}.$$

The discretization of the r -Frobenius norm becomes

$$(\|\mathbf{w}_h\|_{F,r})_i := \left(\sum_{n=1}^m \sum_{k=1}^2 ((\mathbf{w}_h)_{2(n-1)N+(k-1)N+i})^r \right)^{1/r}, \quad \forall i \in \{1, \dots, N\}.$$

Since discrete functions are represented by vectors in a finite difference framework, it is necessary to discretize the corresponding operators as well. We propose to define the discretization T_h of T such that, for a vector v_h , we have $(T_h v_h)_i := (T I_h v_h)(\mathbf{x}_i)$, for $i \in \{1, \dots, N\}$. For our problem (\mathcal{P}) , we represent by $g_h \in \mathbb{R}^N$ the discretization of the data g and let $T_h \in \mathbb{R}^{N \times mN}$, $T_h^* \in \mathbb{R}^{mN \times N}$, $S_h \in \mathbb{R}^{N \times mN}$, $S_h^* \in \mathbb{R}^{mN \times N}$, $\nabla_h \in \mathbb{R}^{2mN \times mN}$, $\nabla_h^* \in \mathbb{R}^{mN \times 2mN}$, $B_h \in \mathbb{R}^{mN \times mN}$ and $B_h^{-1} \in \mathbb{R}^{mN \times mN}$ be the discretization of T , T^* , S , S^* , ∇ , ∇^* , B and B^{-1} respectively. Note

that B_h^{-1} is not necessarily the inverse of B_h . For $\mathbf{w}_h \in \mathbb{R}^{mN}$, we define $\|\mathbf{w}_h\|_{B_h^{-1}}^2 := \langle \mathbf{w}_h, B_h^{-1} \mathbf{w}_h \rangle_{L^2(\Omega_h)^m}$. With the above notations the discretized primal problem reads

$$\min_{\mathbf{v}_h \in \mathbb{R}^{mN}} \left\{ E_h(\mathbf{v}_h) := \alpha_1 \sum_{i=1}^N h_i^2 |(T_h \mathbf{v}_h - g_h)_i| + \frac{\alpha_2}{2} \|T_h \mathbf{v}_h - g_h\|_{L^2(\Omega_h)}^2 + \frac{\beta}{2} \|S_h \mathbf{v}_h\|_{V_{S,h}}^2 + \lambda \sum_{i=1}^N h_i^2 (|\nabla_h \mathbf{v}_h|_{F,r})_i \right\}, \quad (\mathcal{P}_h)$$

where S_h and its associated spaces $V_{S,h}$ can be the following:

- $S_h = Id$, then $V_{S,h} = \mathbb{R}^{mN}$ and $\|\cdot\|_{V_{S,h}} = \|\cdot\|_{L^2(\Omega_h)^m}$,
- $S_h = \nabla_h$, then $V_{S,h} = \mathbb{R}^{2mN}$ and $\|\cdot\|_{V_{S,h}} = \|\cdot\|_{(L^2(\Omega_h)^d)^m}$.

Analogously, the discrete dual problem is given by

$$\max_{(q_{h,1}, \mathbf{q}_{h,2}) \in \mathbb{R}^N \times \mathbb{R}^{2mN}} \left\{ D_h(q_{h,1}, \mathbf{q}_{h,2}) := -\frac{1}{2} \|T_h^* q_{h,1} + \nabla_h^* \mathbf{q}_{h,2} - \alpha_2 T_h^* g_h\|_{B_h^{-1}}^2 + \frac{\alpha_2}{2} \|g_h\|_{L^2(\Omega_h)}^2 - \langle g_h, q_{h,1} \rangle_{L^2(\Omega_h)} - \chi_{|q_{h,1}| \leq \alpha_1} - \chi_{|\mathbf{q}_{h,2}|_{F,s} \leq \lambda} \right\}. \quad (\mathcal{D}_h)$$

Here, the predicate $|q_{h,1}| \leq \alpha_1$ is to be understood as a condition on the degree of freedom, i.e. $|(q_{h,1})_i| \leq \alpha_1$, for all $i = 1, \dots, N$. The same applies for the predicate $|\mathbf{q}_{h,2}|_{F,s} \leq \lambda$.

4 Finite Difference Method on Non-uniform Grid

As traditional finite differences cannot be directly applied to non-uniform grids, we derive in this section a respective finite difference scheme for such grids tailored to discretize gradient and divergence operators. For $\mathbf{x} = (x, y) \in \Omega_h$, we denote by h the length of the element with center \mathbf{x} , and we set $\mathbf{x}_E := (x + h, y) \in \Omega_h$ (see Figure 2(a)) and $\mathbf{x}_S := (x, y + h) \in \Omega_h$ (Figure 2(b)). A simple application of Taylor expansion yields the forward x - and y -derivative of $u \in C^1(\Omega)$ at \mathbf{x} , given by

$$\partial_x u(\mathbf{x}) = \frac{u(\mathbf{x}_E) - u(\mathbf{x})}{h} + O(h) \quad \text{and} \quad \partial_y u(\mathbf{x}) = \frac{u(\mathbf{x}_S) - u(\mathbf{x})}{h} + O(h).$$

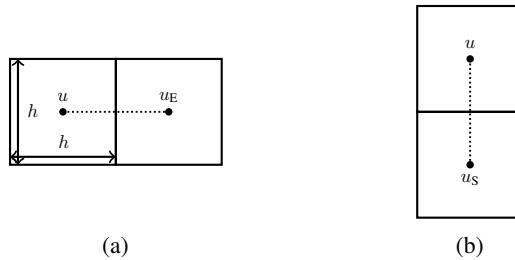


Figure 2: Illustration of a regular node with $u := u(\mathbf{x})$, $u_E := u(\mathbf{x}_E)$ and $u_S := u(\mathbf{x}_S)$.

In the following, we call *dangling nodes* the nodes that have neighbors of a different size than its element's size. Since we assume that neighboring elements are only allowed to be one level finer or coarser, see Figure 1, we end up with 3 different dangling nodes.

We call constellations as depicted in Figure 3 *dangling node 1*. To obtain a finite difference derivative for the situation in Figure 3a, for $\mathbf{x} = (x, y) \in \Omega_h$, we set $\mathbf{x}_{NE} := (x + \frac{3}{4}h, y - \frac{1}{4}h) \in \Omega_h$ and $\mathbf{x}_{SE} := (x + \frac{3}{4}h, y + \frac{1}{4}h) \in \Omega_h$. Applying Taylor expansion, we get

$$u(\mathbf{x}_{NE}) = u(\mathbf{x}) + \frac{3}{4}h \partial_x u(\mathbf{x}) - \frac{1}{4}h \partial_y u(\mathbf{x}) + O(h^2), \quad u(\mathbf{x}_{SE}) = u(\mathbf{x}) + \frac{3}{4}h \partial_x u(\mathbf{x}) + \frac{1}{4}h \partial_y u(\mathbf{x}) + O(h^2).$$

Summing up the latter two equations yields the forward x -derivative of u at \mathbf{x} , given by

$$\partial_x u(\mathbf{x}) = \frac{\frac{u(\mathbf{x}_{NE}) + u(\mathbf{x}_{SE})}{2} - u(\mathbf{x})}{(3/4)h} + O(h).$$

Similarly, by denoting $\mathbf{x}_{SW} := (x - \frac{1}{4}h, y + \frac{3}{4}h) \in \Omega_h$ and $\mathbf{x}_{SE} := (x + \frac{1}{4}h, y + \frac{3}{4}h) \in \Omega_h$ (Figure 3b), the forward y -derivative of u at \mathbf{x} reads

$$\partial_y u(\mathbf{x}) = \frac{\frac{u(\mathbf{x}_{SW}) + u(\mathbf{x}_{SE})}{2} - u(\mathbf{x})}{(3/4)h} + O(h).$$

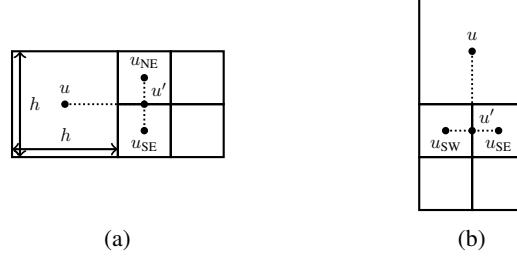


Figure 3: Illustration of a *dangling node 1* with $u := u(\mathbf{x})$. For (a): $u_{NE} := u(\mathbf{x}_{NE})$, $u_{SE} := u(\mathbf{x}_{SE})$ and $u' := \frac{1}{2}(u_{NE} + u_{SE})$. For (b): $u_{SW} := u(\mathbf{x}_{SW})$, $u_{SE} := u(\mathbf{x}_{SE})$ and $u' := \frac{1}{2}(u_{SW} + u_{SE})$.

We call *dangling node 2* the patterns as shown in Figure 4(a) and (b). To determine the finite difference derivative for the case illustrated in Figure 4(a), we set for $(x, y) \in \Omega_h$, $\mathbf{x}_N := (x, y - h) \in \Omega_h$ and $\mathbf{x}_E := (x + \frac{3}{2}h, y - \frac{1}{2}h) \in \Omega_h$. Applying Taylor expansion results in

$$u(\mathbf{x}_N) = u(\mathbf{x}) - h \partial_y u(\mathbf{x}) + O(h^2), \quad (3)$$

$$u(\mathbf{x}_E) = u(\mathbf{x}) + \frac{3}{2}h \partial_x u(\mathbf{x}) - \frac{1}{2}h \partial_y u(\mathbf{x}) + O(h^2). \quad (4)$$

We subtract two times (4) from (3) and we get the forward x -derivative of u at \mathbf{x}

$$\partial_x u(\mathbf{x}) = \frac{2u(\mathbf{x}_E) - u(\mathbf{x}_N) - u(\mathbf{x})}{3h} + O(h).$$

In a similar manner, setting $\mathbf{x}_S := (x + \frac{1}{2}h, y + \frac{3}{2}h) \in \Omega_h$ and $\mathbf{x}_E := (x + h, y) \in \Omega_h$ (Figure 4(b)), we obtain the forward y -derivative of u at \mathbf{x}

$$\partial_y u(\mathbf{x}) = \frac{2u(\mathbf{x}_S) - u(\mathbf{x}_E) - u(\mathbf{x})}{3h} + O(h).$$

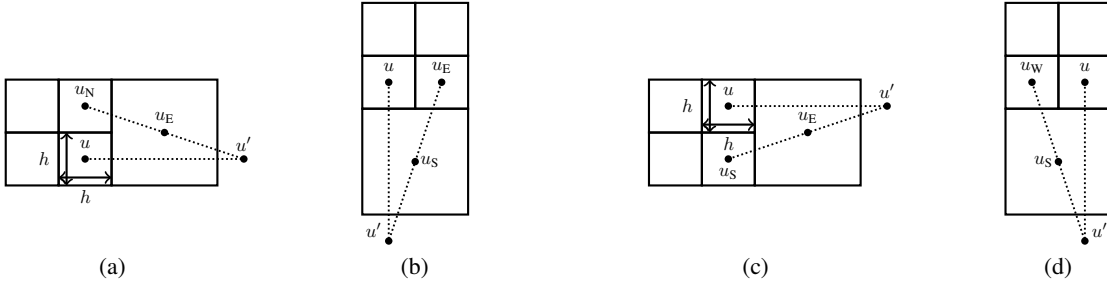


Figure 4: Illustration of a *dangling node 2* (a)-(b) and *dangling node 3* (c)-(d) with $u := u(\mathbf{x})$. For (a): $u_E := u(\mathbf{x}_E)$, $u_N := u(\mathbf{x}_N)$ and $u' := 2u_E - u_N$. For (b): $u_S := u(\mathbf{x}_S)$, $u_E := u(\mathbf{x}_E)$ and $u' := 2u_S - u_E$. For (c): $u_E := u(\mathbf{x}_E)$, $u_S := u(\mathbf{x}_S)$ and $u' := 2u_E - u_S$. For (d): $u_S := u(\mathbf{x}_S)$, $u_W := u(\mathbf{x}_W)$ and $u' := 2u_S - u_W$.

We refer to configurations as depicted in Figure 4(c) and (d) as *dangling node 3*. To calculate a finite difference derivative for the scenario shown in Figure 4(c), we set, for $(x, y) \in \Omega_h$, $\mathbf{x}_S := (x, y + h) \in \Omega_h$ and $\mathbf{x}_E := (x + \frac{3}{2}h, y + \frac{1}{2}h) \in \Omega_h$. We use Taylor expansion, and we obtain the forward x -derivative of u at \mathbf{x} , given by

$$\partial_x u(\mathbf{x}) = \frac{2u(\mathbf{x}_E) - u(\mathbf{x}_S) - u(\mathbf{x})}{3h} + O(h).$$

Likewise, setting $\mathbf{x}_S := (x - \frac{1}{2}h, x + \frac{3}{2}h) \in \Omega_h$ and $\mathbf{x}_W := (x - h, y) \in \Omega_h$ (Figure 4(d)), we have the forward derivative of u with respect to y at \mathbf{x}

$$\partial_y u(\mathbf{x}) = \frac{2u(\mathbf{x}_S) - u(\mathbf{x}_W) - u(\mathbf{x})}{3h} + O(h).$$

To sum up, if we denote $u_\square := u(\mathbf{x}_\square)$ where $\square \in \{N, E, S, W, NE, NW, SE, SW\}$ and h is the length of the element with center $\mathbf{x} \in \Omega_h$, we define $\partial_x^+ u$ as the discrete forward x -derivative of u at \mathbf{x} , $\partial_y^+ u$ as the discrete forward y -derivative of u at \mathbf{x} , $\partial_x^- u$ as the discrete backward x -derivative of u at \mathbf{x} and $\partial_y^- u$ as the discrete backward y -derivative of u at \mathbf{x} by:

- on *regular node* (Figure 2):

$$\partial_x^+ u = \frac{u_E - u}{h}, \quad \partial_y^+ u = \frac{u_S - u}{h}, \quad \text{and} \quad \partial_x^- u = \frac{u - u_W}{h}, \quad \partial_y^- u = \frac{u - u_N}{h}.$$

- on *dangling node 1* (Figure 3):

$$\partial_x^+ u = \frac{\frac{u_{NE} + u_{SE}}{2} - u}{(3/4)h}, \quad \partial_y^+ u = \frac{\frac{u_{SW} + u_{SE}}{2} - u}{(3/4)h}, \quad \text{and} \quad \partial_x^- u = \frac{u - \frac{u_{NW} + u_{SW}}{2}}{(3/4)h}, \quad \partial_y^- u = \frac{u - \frac{u_{NW} + u_{NE}}{2}}{(3/4)h}.$$

- on *dangling node 2* (Figure 4(a) and (b)):

$$\partial_x^+ u = \frac{2u_E - u_N - u}{3h}, \quad \partial_y^+ u = \frac{2u_S - u_E - u}{3h}, \quad \text{and} \quad \partial_x^- u = \frac{u - 2u_W + u_N}{3h}, \quad \partial_y^- u = \frac{u - 2u_N + u_E}{3h}.$$

- on *dangling node 3* (Figure 4(c) and (d)):

$$\partial_x^+ u = \frac{2u_E - u_S - u}{3h}, \quad \partial_y^+ u = \frac{2u_S - u_W - u}{3h}, \quad \text{and} \quad \partial_x^- u = \frac{u - 2u_W + u_S}{3h}, \quad \partial_y^- u = \frac{u - 2u_N + u_W}{3h}.$$

We define the discrete gradient operator ∇_h by the concatenation of the forward x -derivative and the y -derivative described above for all $\mathbf{x} \in \Omega_h$, i.e. $\nabla_h := (\partial_x^+ \ \partial_y^+)^T$. Similarly, we define the discrete divergence operator div_h by $\text{div}_h := (\partial_x^- \ \partial_y^-)$.

On a uniform mesh in our discrete setting, the gradient and divergence operators are adjoint to each other, just as they are in the continuous case, i.e. we have $(\nabla_h)^* = -\text{div}_h$ when adding homogeneous Neumann boundaries condition on the discrete gradient and homogeneous Dirichlet boundaries condition on the discrete divergence. However, on non-uniform meshes, the discrete gradient and divergence operators are no longer adjoint. Indeed, let us consider the grid in Figure 1. In this particular example one can compute the discrete operators for $m = 1$, and show that $(\nabla_h)^* = (\nabla_h)^T \neq -\text{div}_h = (\nabla^*)_h$. Note that the order of the operations matters: discretizing and computing the adjoint is different from taking the adjoint and then discretize.

Based on the above derived forward and backward finite differences on non-uniform grids, we additionally propose centered finite difference schemes for non-uniform grids. In particular, these centered finite difference schemes ∂_x^c and ∂_y^c are defined as the average of the forward and backward difference scheme, i.e.

$$\partial_x^c := \frac{1}{2}(\partial_x^+ + \partial_x^-) \quad \text{and} \quad \partial_y^c := \frac{1}{2}(\partial_y^+ + \partial_y^-).$$

5 Impact of Refinement on the Total Variation

In [18] it has been shown that the discrete total variation is dependent on the number of points in the discrete domain Ω_h . Here, we aim to quantify the change of the discrete total variation with respect to the grid. Let Ω_h be any quad-mesh and let us consider its one-time refinement (we refine at most once every element) $\widetilde{\Omega}_h$ (see for instance Figure 5). We denote by I (resp. \widetilde{I}) the set of indices $\{1, \dots, N\}$ (resp. $\{1, \dots, \widetilde{N}\}$), where N (resp. \widetilde{N}) is the number of degree of freedom of Ω_h (resp. $\widetilde{\Omega}_h$). For vectors $\mathbf{u}_h \in \mathbb{R}^{mN}$ and $\widetilde{\mathbf{u}}_h \in \mathbb{R}^{m\widetilde{N}}$, we define respective discrete (weighted) total variations by

$$\text{TV}(\mathbf{u}_h) := \sum_{i \in I} h_i^2 (|\nabla_h \mathbf{u}_h|_{F,r})_i, \quad \text{and} \quad \widetilde{\text{TV}}_\mu(\widetilde{\mathbf{u}}_h) := \sum_{i \in \widetilde{I}} \widetilde{h}_i^2 \mu_i (|\widetilde{\nabla}_h \widetilde{\mathbf{u}}_h|_{F,r})_i,$$

where $\mu \in \mathbb{R}^{\widetilde{N}}$ and $\widetilde{\nabla}_h, \widetilde{\nabla}_h$ are any suitable discrete gradient on Ω_h and on $\widetilde{\Omega}_h$. We denote by \mathcal{R} the set of indices of elements of Ω_h that have been refined to create the mesh $\widetilde{\Omega}_h$ and we denote by \mathcal{N} the indices of the refined elements

and their neighbors (north, east, south and west), i.e. $\mathcal{N} := \{i \in I \mid \exists j \in \mathcal{R}, E_i \text{ share an edge with } E_j\}$. Thus we can write

$$\text{TV}(\mathbf{u}_h) = \sum_{i \in I \setminus \mathcal{N}} h_i^2 (|\nabla_h \mathbf{u}_h|_{F,r})_i + \sum_{i \in \mathcal{N} \setminus \mathcal{R}} h_i^2 (|\nabla_h \mathbf{u}_h|_{F,r})_i + \sum_{i \in \mathcal{R}} h_i^2 (|\nabla_h \mathbf{u}_h|_{F,r})_i.$$

We define the mapping $\tilde{\sigma}$ which maps the indices of an element of Ω_h to the indices of the corresponding (or the 4 corresponding) element(s) of $\tilde{\Omega}_h$, i.e. for $i \in I$

$$\tilde{\sigma}(i) = \begin{cases} \{i\}, & \text{if } i \notin \mathcal{R}, \\ \{i_1, i_2, i_3, i_4\}, & \text{if } i \in \mathcal{R}, \end{cases}$$

where $i_k \in \tilde{I}$, $k = 1, \dots, 4$, are the indices of the sub-elements. For $J \subseteq I$, let us define $\tilde{\sigma}(J) = \bigcup_{j \in J} \tilde{\sigma}(j)$. Note that $\tilde{I} = \tilde{\sigma}(I) = \tilde{\sigma}((I \setminus \mathcal{N}) \cup (\mathcal{N} \setminus \mathcal{R}) \cup \mathcal{R}) = \tilde{\sigma}(I \setminus \mathcal{N}) \cup \tilde{\sigma}(\mathcal{N} \setminus \mathcal{R}) \cup \tilde{\sigma}(\mathcal{R}) = (I \setminus \mathcal{N}) \cup (\mathcal{N} \setminus \mathcal{R}) \cup \tilde{\sigma}(\mathcal{R})$. Since $\tilde{h}_i = h_i$ for $i \in I \setminus \mathcal{R}$ and $\tilde{h}_i = \frac{h_i}{2}$ for $i \in \mathcal{R}$, we obtain

$$\begin{aligned} \widetilde{\text{TV}}_\mu(\tilde{\mathbf{u}}_h) &= \sum_{i \in I \setminus \mathcal{N}} \tilde{h}_i^2 \mu_i (|\widetilde{\nabla}_h \tilde{\mathbf{u}}_h|_{F,r})_i + \sum_{i \in \mathcal{N} \setminus \mathcal{R}} \tilde{h}_i^2 \mu_i (|\widetilde{\nabla}_h \tilde{\mathbf{u}}_h|_{F,r})_i + \sum_{i \in \tilde{\sigma}(\mathcal{R})} \tilde{h}_i^2 \mu_i (|\widetilde{\nabla}_h \tilde{\mathbf{u}}_h|_{F,r})_i \\ &= \sum_{i \in I \setminus \mathcal{N}} h_i^2 \mu_i (|\widetilde{\nabla}_h \tilde{\mathbf{u}}_h|_{F,r})_i + \sum_{i \in \mathcal{N} \setminus \mathcal{R}} h_i^2 \mu_i (|\widetilde{\nabla}_h \tilde{\mathbf{u}}_h|_{F,r})_i + \sum_{i \in \mathcal{R}} \frac{h_i^2}{4} \sum_{k=1}^4 \mu_{i_k} (|\widetilde{\nabla}_h \tilde{\mathbf{u}}_h|_{F,r})_{i_k}. \end{aligned}$$

We denote by $\pi : \mathbb{R}^N \rightarrow \mathbb{R}^{\tilde{N}}$ the projection of a discrete function on Ω_h into $\tilde{\Omega}_h$ and by $\tilde{\pi} : \mathbb{R}^{\tilde{N}} \rightarrow \mathbb{R}^N$ the projection of a discrete function on $\tilde{\Omega}_h$ into Ω_h . More precisely, for $i \in I$

$$(\pi \mathbf{u}_h)_j = (\mathbf{u}_h)_i, \text{ for } j \in \tilde{\sigma}(i) \quad \text{and} \quad (\tilde{\pi} \tilde{\mathbf{u}}_h)_i = \frac{1}{\#\tilde{\sigma}(i)} \sum_{j \in \tilde{\sigma}(i)} (\tilde{\mathbf{u}}_h)_j,$$

where $\#\tilde{\sigma}(i)$ is the cardinality of $\tilde{\sigma}(i)$. Then, using that $(|\widetilde{\nabla}_h \pi \mathbf{u}_h|_{F,r})_i = (|\nabla_h \mathbf{u}_h|_{F,r})_i$, for $i \in I \setminus \mathcal{N}$, it yields

$$\begin{aligned} \text{TV}(\mathbf{u}_h) - \widetilde{\text{TV}}_\mu(\pi \mathbf{u}_h) &= \sum_{i \in I \setminus \mathcal{N}} h_i^2 (|\nabla_h \mathbf{u}_h|_{F,r})_i + \sum_{i \in \mathcal{N} \setminus \mathcal{R}} h_i^2 (|\nabla_h \mathbf{u}_h|_{F,r})_i + \sum_{i \in \mathcal{R}} h_i^2 (|\nabla_h \mathbf{u}_h|_{F,r})_i \\ &\quad - \sum_{i \in I \setminus \mathcal{N}} h_i^2 \mu_i (|\widetilde{\nabla}_h \pi \mathbf{u}_h|_{F,r})_i - \sum_{i \in \mathcal{N} \setminus \mathcal{R}} h_i^2 \mu_i (|\widetilde{\nabla}_h \pi \mathbf{u}_h|_{F,r})_i \\ &\quad - \sum_{i \in \mathcal{R}} \frac{h_i^2}{4} \sum_{k=1}^4 \mu_{i_k} (|\widetilde{\nabla}_h \pi \mathbf{u}_h|_{F,r})_{i_k} \\ &= \sum_{i \in I \setminus \mathcal{N}} h_i^2 (1 - \mu_i) (|\nabla_h \mathbf{u}_h|_{F,r})_i + \sum_{i \in \mathcal{N} \setminus \mathcal{R}} h_i^2 ((|\nabla_h \mathbf{u}_h|_{F,r})_i - \mu_i (|\widetilde{\nabla}_h \pi \mathbf{u}_h|_i)) \\ &\quad + \sum_{i \in \mathcal{R}} h_i^2 \left((|\nabla_h \mathbf{u}_h|_{F,r})_i - \frac{1}{4} \sum_{k=1}^4 \mu_{i_k} (|\widetilde{\nabla}_h \pi \mathbf{u}_h|_{F,r})_{i_k} \right). \end{aligned}$$

In order to see the quantitative change of the discrete total variation we need to seek for μ such that $\text{TV}(\mathbf{u}_h) - \widetilde{\text{TV}}_\mu(\pi \mathbf{u}_h) = 0$. For that, we suppose that μ is constant on every element of Ω_h , in particular, we have $\mu_{i_k} =: \mu_i$ for $i \in \mathcal{R}$ and $k = 1, 2, 3, 4$. Then

$$\begin{aligned} \text{TV}(\mathbf{u}_h) - \widetilde{\text{TV}}_\mu(\pi \mathbf{u}_h) &= \sum_{i \in I \setminus \mathcal{N}} h_i^2 (1 - \mu_i) (|\nabla_h \mathbf{u}_h|_{F,r})_i + \sum_{i \in \mathcal{N} \setminus \mathcal{R}} h_i^2 ((|\nabla_h \mathbf{u}_h|_{F,r})_i - \mu_i (|\widetilde{\nabla}_h \pi \mathbf{u}_h|_{F,r})_i) \\ &\quad + \sum_{i \in \mathcal{R}} h_i^2 \left((|\nabla_h \mathbf{u}_h|_{F,r})_i - \mu_i \frac{1}{4} \sum_{k=1}^4 (|\widetilde{\nabla}_h \pi \mathbf{u}_h|_{F,r})_{i_k} \right). \end{aligned}$$

The above expression vanishes if the following system of equations holds:

$$\begin{cases} (1 - \mu_i) (|\nabla_h \mathbf{u}_h|_{F,r})_i = 0, & i \in I \setminus \mathcal{N}, \\ (|\nabla_h \mathbf{u}_h|_{F,r})_i - \mu_i (|\widetilde{\nabla}_h \pi \mathbf{u}_h|_{F,r})_i = 0, & i \in \mathcal{N} \setminus \mathcal{R}, \\ (|\nabla_h \mathbf{u}_h|_{F,r})_i - \frac{1}{4} \mu_i \sum_{k=1}^4 (|\widetilde{\nabla}_h \pi \mathbf{u}_h|_{F,r})_{i_k} = 0, & i \in \mathcal{R}. \end{cases}$$

These equations are satisfied if (note that $(\widetilde{\pi}|\widetilde{\nabla}_h\pi\mathbf{u}_h|_{F,r})_i = 0$ if and only if $(|\nabla_h\mathbf{u}_h|_{F,r})_i = 0$)

$$\mu_i := \begin{cases} \frac{(|\nabla_h\mathbf{u}_h|_{F,r})_i}{(\widetilde{\pi}|\widetilde{\nabla}_h\pi\mathbf{u}_h|_{F,r})_i}, & \text{if } (\widetilde{\pi}|\widetilde{\nabla}_h\pi\mathbf{u}_h|_{F,r})_i \neq 0, \\ 1, & \text{otherwise.} \end{cases} \quad (5)$$

for all $i \in I$. Indeed, if $i \in I \setminus \mathcal{N}$, then $(|\nabla_h\mathbf{u}_h|_{F,r})_i = (\widetilde{\pi}|\widetilde{\nabla}_h\pi\mathbf{u}_h|_{F,r})_i$ and hence $\mu_i = 1$, otherwise, if $i \in \mathcal{N} \setminus \mathcal{R}$, then we have $(\widetilde{\pi}|\widetilde{\nabla}_h\pi\mathbf{u}_h|_{F,r})_i = (|\nabla_h\pi\mathbf{u}_h|_{F,r})_i$. Finally, $(\widetilde{\pi}|\widetilde{\nabla}_h\pi\mathbf{u}_h|_{F,r})_i = \frac{1}{4} \sum_{k=1}^4 (|\widetilde{\nabla}_h\pi\mathbf{u}_h|_{F,r})_{i_k}$ if $i \in \mathcal{R}$. Therefore, for an adaptive grid, refining elements of the mesh may impact the value of the total variation. In fact, the continuous total variation of a function f differs in general from the discrete total variation of the discretized f .

Example. Let us study the particular case where $m = 1$.

(a) We suppose that $\widetilde{\Omega}_h$ is a global refinement of the uniform mesh Ω_h . On the uniform mesh, we use the multi-indices $i = (a, b)$ to identify an element of Ω_h and the multi-index $i_k = (a, b, k)$ with $k = 1, 2, 3, 4$, to identify a sub-element of $\widetilde{\Omega}_h$. The forward finite difference scheme writes (we write $u_{a,b}$ instead of $(\mathbf{u}_h)_{a,b}$)

$$(|\nabla_h\mathbf{u}_h|_r)_{a,b} = \frac{1}{h} (|u_{a+1,b} - u_{a,b}|^r + |u_{a,b+1} - u_{a,b}|^r)^{1/r},$$

and

$$\begin{aligned} (|\widetilde{\nabla}_h\pi\mathbf{u}_h|_r)_{a,b,1} &= 0, & (|\widetilde{\nabla}_h\pi\mathbf{u}_h|_r)_{a,b,2} &= \frac{2}{h} |u_{a+1,b} - u_{a,b}|, \\ (|\widetilde{\nabla}_h\pi\mathbf{u}_h|_r)_{a,b,3} &= \frac{2}{h} |u_{a,b+1} - u_{a,b}|, & (|\widetilde{\nabla}_h\pi\mathbf{u}_h|_r)_{a,b,4} &= \frac{2}{h} (|u_{a+1,b} - u_{a,b}|^r + |u_{a,b+1} - u_{a,b}|^r)^{1/r}. \end{aligned}$$

Then

$$(\widetilde{\pi}|\widetilde{\nabla}_h\pi\mathbf{u}_h|_r)_{a,b} = \frac{1}{2h} |u_{a+1,b} - u_{a,b}| + \frac{1}{2h} |u_{a,b+1} - u_{a,b}| + \frac{1}{2h} (|u_{a+1,b} - u_{a,b}|^r + |u_{a,b+1} - u_{a,b}|^r)^{1/r}.$$

If $r = 1$ (anisotropic total variation), we have $\mu_{a,b} = 1$. Therefore, for a uniform grid, the size of the elements of the mesh have no impact on the value of the anisotropic total variation. If $r = 2$ (isotropic total variation), using the above computations, we obtain if $\sqrt{(u_{a+1,b} - u_{a,b})^2} + \sqrt{(u_{a,b+1} - u_{a,b})^2} + \sqrt{(u_{a+1,b} - u_{a,b})^2 + (u_{a,b+1} - u_{a,b})^2} \neq 0$

$$0 < \mu_{a,b} = \frac{2\sqrt{(u_{a+1,b} - u_{a,b})^2 + (u_{a,b+1} - u_{a,b})^2}}{\sqrt{(u_{a+1,b} - u_{a,b})^2} + \sqrt{(u_{a,b+1} - u_{a,b})^2} + \sqrt{(u_{a+1,b} - u_{a,b})^2 + (u_{a,b+1} - u_{a,b})^2}} \leq 1,$$

and the size of the elements of the mesh indeed have impact on the value of the isotropic total variation, in particular, it increases its value. Hence, the solution of the discrete problem (\mathcal{P}_h) depends on the mesh-size.

(b) Now we consider any grid Ω_h and its refinement $\widetilde{\Omega}_h$, not necessarily uniform. If $r = 1$, let us consider the grid Ω_h on Figure 5, and an associated one-time refined grid $\widetilde{\Omega}_h$. Simple computations give $\mu_{1,1} = 1$, $\mu_{1,2} = \frac{3}{4}$ if $u_{2,2} \neq u_{1,2}$,



Figure 5: One refinement example with Ω_h on the left and a one-refinement $\widetilde{\Omega}_h$ on the right.

$\mu_{2,1} = \frac{3}{4}$ if $u_{2,2} \neq u_{2,1}$ and $\mu_{2,2} = 1$, which means that the total variation is changing after refinement. If $r = 2$, this result is also true for any (non)-uniform grid since it always contains some uniform parts (if the function is not constant on the uniform part of the grid).

In practice, we look at a fixed discrete data g and refining the grid alters the balance between the total variation and the other terms in the discrete problem. In order to compensate this change of energy, one could change the value of the parameter according to (5). However, we note that while (5) is compensating the change of the discrete total variation, it leads to a locally weighted total variation, where the weights are chosen considering only very local (one pixel) information. Hence, compensating with (5) in total variation minimization should only be used with caution as a very local criterion might lead to a very dramatic change of the weight from one pixel to the next introducing artifacts in the restoration, as we observed it in numerical experiments. Note that locally adaptive parameter strategies for total variation minimization, as in [20, 24, 30, 32], consider overlapping windows of reasonable size to establish a local parameter for total variation minimization. This avoids a dramatic change of the local weights and helps to avoid artifacts.

6 Primal-Dual Gap Error Estimator

In this section we derive an indicator for the mesh adaptivity, namely the primal-dual gap error estimator. For the continuous problem we have strong duality [21, Theorem 4.2, Chapter 3], namely, if \mathbf{u} is a solution of (\mathcal{P}) and (p_1, \mathbf{p}_2) is a solution of (\mathcal{D}) , we have $E(\mathbf{u}) = D(p_1, \mathbf{p}_2)$. However, for non-uniform grids, this last statement might not be true as the discrete gradient ∇_h is not the adjoint of the discrete divergence div_h . We have the following primal-dual gap error, whose proof is provided in Appendix A:

Proposition 6.1. *Let $\mathbf{u} \in H^1(\Omega)^m$ be a solution of (\mathcal{P}) and $\mathbf{u}_h \in \mathbb{R}^{mN}$ be a solution of (\mathcal{P}_h) . Then, for all $\mathbf{v}_h \in \mathbb{R}^{mN}$ and $(q_{h,1}, \mathbf{q}_{h,2}) \in \mathbb{R}^N \times \mathbb{R}^{2mN}$, we have*

$$\frac{1}{2} \|I_h \mathbf{u}_h - \mathbf{u}\|_B^2 \leq \eta_h(\mathbf{v}_h, q_{h,1}, \mathbf{q}_{h,2}) + c \|I_h g_h - g\|_{L^2(\Omega)} + R_h(\mathbf{u}_h) + Q_h(p_{h,1}, \mathbf{p}_{h,2}),$$

where $c \geq 0$ and

$$\eta_h(\mathbf{v}_h, q_{h,1}, \mathbf{q}_{h,2}) := E_h(\mathbf{v}_h) - D_h(q_{h,1}, \mathbf{q}_{h,2}),$$

$$R_h(\mathbf{u}_h) := E(I_h \mathbf{u}_h) - E_h(\mathbf{u}_h),$$

$$Q_h(p_{h,1}, \mathbf{p}_{h,2}) := \frac{1}{2} \left(\|T^* I_h p_{h,1} + \nabla^* I_h \mathbf{p}_{h,2} + \alpha_2 T^* g\|_{B^{-1}}^2 - \|T_h^* q_{h,1} + \nabla_h^* \mathbf{q}_{h,2} - \alpha_2 T_h^* g_h\|_{B_h^{-1}}^2 \right).$$

We notice that

$$\begin{aligned} E(I_h \mathbf{u}_h) - E_h(\mathbf{u}_h) &= \alpha_1 \left(\int_{\Omega} |T I_h \mathbf{u}_h - g| dx - \sum_{i=1}^N h_i^2 (|T_h \mathbf{u}_h - g_h|)_i \right) \\ &\quad + \frac{\alpha_2}{2} \left(\|T I_h \mathbf{u}_h - g\|_{L^2(\Omega)}^2 - \|T_h \mathbf{u}_h - g_h\|_{L^2(\Omega_h)}^2 \right) + \frac{\beta}{2} \left(\|S I_h \mathbf{u}_h\|_{V_S}^2 - \|S_h \mathbf{u}_h\|_{V_{S,h}}^2 \right) \\ &\quad + \lambda \left(\int_{\Omega} |\nabla I_h \mathbf{u}_h|_{F,r} dx - \sum_{i=1}^N h_i^2 (|\nabla_h \mathbf{u}_h|_{F,r})_i \right). \end{aligned}$$

In general, $T I_h u_h$ and $S I_h u_h$ are not piecewise constant despite $I_h u_h$ is. That is why, for example, the second term becomes

$$\|T I_h \mathbf{u}_h - g\|_{L^2(\Omega)}^2 - \|T_h \mathbf{u}_h - g_h\|_{L^2(\Omega_h)}^2 = \sum_{i=1}^N \int_{E_i} (T I_h \mathbf{u}_h - g)^2 - ((T I_h \mathbf{u}_h)(\mathbf{x}_i) - I_h g_h(x))^2 dx,$$

where E_i is the i -th element of the mesh, h_i is its length and \mathbf{x}_i is its center. A similar behavior occurs for the first and third terms. In fact, these terms represent the discretization error of the operators T and S and of the data g . The term $\int_{\Omega} |\nabla I_h \mathbf{u}_h|_{F,r} dx - \sum_{i=1}^N h_i^2 (|\nabla_h \mathbf{u}_h|_{F,r})_i$ corresponds to the discretization error of the total variation. In the piecewise constant setting, it has been proved that this term does not go to 0 when h tends to 0 [6]. It is the reason why we do not expect the term $E(I_h \mathbf{u}_h) - E_h(\mathbf{u}_h)$ to go to 0 when h goes to 0 and why we do not include this term in our mesh refinement indicator.

The term Q_h is the discretization error of the operators and of the data term g . In general, we do not have $(B^{-1})_h = (B_h)^{-1}$ and $(B^{-1} T^*)_h = (B^{-1})_h (T^*)_h$. Moreover, we may have to assume the convergence of the discrete operators to the continuous one in suitable senses. That is why the study of Q_h is difficult and may be the topic of further research. Consequently, we chose not to use $D(I_h p_{h,1}, I_h \mathbf{p}_{h,2}) - D_h(p_{h,1}, \mathbf{p}_{h,2})$ in our refinement indicator.

As a consequence of the previous proposition, we use a local version $(\eta_h)_i$ of η_h , i.e. such that $\eta_h = \sum_{i=1}^N (\eta_h)_i$, as indicator for the grid adaptivity defined as: for all $\mathbf{v}_h \in \mathbb{R}^{mN}$ and $(q_{h,1}, \mathbf{q}_{h,2}) \in \mathbb{R}^N \times \mathbb{R}^{2mN}$ such that $|q_{h,1}| \leq \alpha_1$ and $|\mathbf{q}_{h,2}|_{F,s} \leq \lambda$

$$\begin{aligned} h_i^{-2} (\eta_h)_i &= \alpha_1 |(T_h \mathbf{v}_h - g_h)_i| + \frac{\alpha_2}{2} (T_h \mathbf{v}_h - g_h)_i^2 + \frac{\beta}{2} \Phi_i(\mathbf{v}_h) + \lambda (|\nabla_h \mathbf{v}_h|_{F,r})_i \\ &\quad + \frac{1}{2} (T_h^* q_{h,1} + \nabla_h^* \mathbf{q}_{h,2} - \alpha_2 T_h^* g_h)_i (B_h^{-1} (T_h^* q_{h,1} + \nabla_h^* \mathbf{q}_{h,2} - \alpha_2 T_h^* g_h))_i - \frac{\alpha_2}{2} (g_h)_i^2 + (g_h)_i (q_{h,1})_i, \quad (6) \end{aligned}$$

where

$$\Phi_i(\mathbf{v}_h) := \begin{cases} \sum_{k=1}^m (\mathbf{v}_h)_{(k-1)N+i}^2 & \text{if } S_h = Id, \\ \sum_{k=1}^m \sum_{k=1}^2 (\nabla_h \mathbf{v}_h)_{2(n-1)N+(k-1)N+i}^2 & \text{if } S_h = \nabla_h, \end{cases} \quad (7)$$

for $i = 1, \dots, N$.

7 Semi-Smooth Newton Method

In this section we derive a semi-smooth Newton iteration in order to solve the L^1 - L^2 -TV problem. While the dual problem (\mathcal{D}) is concave, its solution may not be unique due to the non-trivial kernel of ∇^* . To ensure a unique solution, we introduce regularization terms for p_1 and \mathbf{p}_2 with corresponding parameters $\gamma_1, \gamma_2 \geq 0$. By setting $\gamma_1, \gamma_2 > 0$, we guarantee the strong concavity of the dual energy [23]. The modified dual problem then becomes

$$\sup_{\mathbf{p}=(p_1, \mathbf{p}_2) \in L^2(\Omega) \times (L^2(\Omega)^d)^m} D(p_1, \mathbf{p}_2) - \frac{\gamma_1}{2\alpha_1} \|p_1\|_{L^2(\Omega)}^2 - \frac{\gamma_2}{2\lambda} \|\mathbf{p}_2\|_{(L^2(\Omega)^d)^m}^2. \quad (8)$$

As in [23], we use the convention that the terms $\frac{\gamma_1}{2\alpha_1} \|p_1\|_{L^2(\Omega)}^2$ and $\frac{\gamma_2}{2\lambda} \|\mathbf{p}_2\|_{(L^2(\Omega)^d)^m}^2$ vanish respectively for $\alpha_1 = 0$ or $\lambda = 0$, as these immediately imply $p_1 = 0$ or $\mathbf{p}_2 = 0$ respectively. By [23, Theorem 3.1 and Proposition 3.2] the dual problem to (8) is given by

$$\inf_{\mathbf{u} \in H^1(\Omega)^m} \alpha_1 \int_{\Omega} \varphi_{\gamma_1}(|T\mathbf{u} - g|) dx + \frac{\alpha_2}{2} \|T\mathbf{u} - g\|_{L^2(\Omega)}^2 + \frac{\beta}{2} \|\mathbf{S}\mathbf{u}\|_{V_S}^2 + \lambda \int_{\Omega} \varphi_{\gamma_2}(|\nabla \mathbf{u}|_{F,r}) dx, \quad (9)$$

where $\varphi_{\gamma} : \mathbb{R} \rightarrow [0, +\infty[$ is the Hubert function defined for $\gamma \geq 0$ as

$$\varphi_{\gamma}(x) := \begin{cases} \frac{1}{2\gamma} x^2, & \text{if } |x| \leq \gamma, \\ |x| - \frac{\gamma}{2}, & \text{otherwise.} \end{cases}$$

The optimality conditions for a solution \mathbf{u} of (9) and a solution (p_1, \mathbf{p}_2) of (8) read

$$\begin{cases} 0 = T^*p_1 + \nabla^* \mathbf{p}_2 - \alpha_2 T^*g + B\mathbf{u}, \\ 0 = p_1 \max\{\gamma_1, |T\mathbf{u} - g|\} - \alpha_1(T\mathbf{u} - g), & \text{if } |p_1| \leq \alpha_1, \\ 0 = \mathbf{p}_2 \max\{\gamma_2, |\nabla \mathbf{u}|_{F,r}\} - \lambda \nabla \mathbf{u}, & \text{if } |\mathbf{p}_2|_{F,r} \leq \lambda. \end{cases} \quad (10)$$

We restrict ourselves to $r = 2$ until the end of the article so that the max-operator and the r -Frobenius norm are generalized differentiable and semi-smooth, justifying the application of a Newton step [27]. When $|p_1| \leq \alpha_1$ and $|\mathbf{p}_2|_{F,r} \leq \lambda$, we have by using the optimality conditions (10)

$$F(\mathbf{u}, p_1, \mathbf{p}_2) := T^*p_1 + \nabla^* \mathbf{p}_2 - \alpha_2 T^*g + B\mathbf{u} + m_1(\mathbf{u})p_1 - \alpha_1(T\mathbf{u} - g) + m_2(\mathbf{u})\mathbf{p}_2 - \lambda \nabla \mathbf{u} = 0, \quad (11)$$

where $m_1(\mathbf{u}) := \max\{\gamma_1, |T\mathbf{u} - g|\}$ and $m_2(\mathbf{u}) := \max\{\gamma_2, |\nabla \mathbf{u}|_{F,r}\}$. The resulting Newton system $(0, 0, 0) = DF(\mathbf{u}, p_1, \mathbf{p}_2)(\mathbf{d}_u, d_{p_1}, \mathbf{d}_{p_2})$ reads as follows:

$$\begin{cases} B\mathbf{d}_u & + T^*d_{p_1} & + \nabla^* \mathbf{d}_{p_2} & = & - \left(\nabla^* \mathbf{p}_2 + T^*p_1 + B\mathbf{u} - \alpha_2 T^*g \right), \\ \chi_1 \frac{(T\mathbf{u}-g) \cdot T\mathbf{d}_u}{|T\mathbf{u}-g|} p_1 - \alpha_1 T\mathbf{d}_u & + m_1 d_{p_1} & & = & - \left(m_1 p_1 - \alpha_1 (T\mathbf{u} - g) \right), \\ \chi_2 \frac{\nabla \mathbf{u} \cdot \nabla \mathbf{d}_u}{|\nabla \mathbf{u}|_{F,r}} \mathbf{p}_2 - \lambda \nabla \mathbf{d}_u & & + m_2 \mathbf{d}_{p_2} & = & - \left(m_2 \mathbf{p}_2 - \lambda \nabla \mathbf{u} \right), \end{cases}$$

where $\mathbf{u} \in H^1(\Omega)^m$, $p_1 \in L^2(\Omega)$, $\mathbf{p}_2 \in (L^2(\Omega)^2)^d$ represent the variables from the previous Newton step and $(\mathbf{d}_u, d_{p_1}, \mathbf{d}_{p_2}) \in H^1(\Omega)^m \times L^2(\Omega) \times (L^2(\Omega)^2)^d$ is the solution of the Newton system. Using the previous equations and by using the definitions of m_1 and m_2 we have

$$d_{p_1} = -p_1 + \frac{\alpha_1}{m_1(\mathbf{u})} (T(\mathbf{u} + \mathbf{d}_u) - g) - \chi_1 \frac{(T\mathbf{u} - g) \cdot T\mathbf{d}_u}{m_1(\mathbf{u})^2} p_1, \quad (12)$$

$$\mathbf{d}_{p_2} = -\mathbf{p}_2 + \frac{\lambda}{m_2(\mathbf{u})} \nabla(\mathbf{u} + \mathbf{d}_u) - \chi_2 \frac{\nabla \mathbf{u} \cdot \nabla \mathbf{d}_u}{m_2(\mathbf{u})^2} \mathbf{p}_2, \quad (13)$$

where

$$\chi_1(\mathbf{u}) := \begin{cases} 1 & \text{if } |T\mathbf{u} - g| \geq \gamma_1, \\ 0 & \text{otherwise,} \end{cases} \quad \text{and} \quad \chi_2(\mathbf{u}) := \begin{cases} 1 & \text{if } |\nabla \mathbf{u}|_{F,r} \geq \gamma_2, \\ 0 & \text{otherwise.} \end{cases}$$

Replacing these two equations into the Newton system gives us

$$H\mathbf{d}_{\mathbf{u}} = G, \quad (14)$$

where

$$H := T^* \left(\frac{\alpha_1}{m_1(\mathbf{u})} T - \chi_1 p_1 \frac{(T\mathbf{u} - g) \cdot T}{m_1(\mathbf{u})^2} \right) + \nabla^* \left(\frac{\lambda}{m_2(\mathbf{u})} \nabla - \chi_2 \mathbf{p}_2 \frac{\nabla \mathbf{u} \cdot \nabla}{m_2(\mathbf{u})^2} \right) + B,$$

and

$$G := -\nabla^* \frac{\lambda}{m_2(\mathbf{u})} \nabla \mathbf{u} - T^* \frac{\alpha_1}{m_1(\mathbf{u})} (T\mathbf{u} - g) - B\mathbf{u} + \alpha_2 T^* g.$$

Now we discretize (12), (13) and (14) using the adaptive finite difference scheme introduced in Section 4. Let $m_{h,1}, m_{h,2} \in \mathbb{R}^N$ represent the approximations of m_1 and m_2 respectively, and let $\chi_{h,1}, \chi_{h,2} \in \mathbb{R}^N$ be the corresponding approximations of χ_1 and χ_2 respectively, as described in Section 3. Then the discrete version of (14) is

$$H_h \mathbf{d}_{\mathbf{u}_h} = G_h, \quad (15)$$

where

$$\begin{aligned} H_h := & B_h + T_h^* D_N(m_{h,1})^{-1} \left(D_N(\alpha_1 \mathbf{1}_N) - D_N(\chi_{h,1}) D_N(m_{h,1})^{-1} D_N(p_{h,1}) D_N(T_h \mathbf{u}_h - g_h) \right) T_h \\ & + \nabla_h^* D_{2N}(m_{h,2})^{-1} \left(D_{2N}(\lambda \mathbf{1}_{2N}) - D_{2N}(\chi_{h,2}) D_{2N}(m_{h,2})^{-1} D_{2N}(\mathbf{p}_{h,2}) \mathcal{N}(\nabla_h \mathbf{u}_h) \right) \nabla_h, \end{aligned}$$

$G_h := -\nabla_h^* D_{2N}(\lambda \mathbf{1}_{2N}) D_{2N}(m_{h,2})^{-1} \nabla_h \mathbf{u}_h - T_h^* D_N(\alpha_1 \mathbf{1}_N) D_N(m_{h,1})^{-1} (T_h \mathbf{u}_h - g_h) - B_h \mathbf{u}_h + D_N(\alpha_2 \mathbf{1}_N) T_h^* g_h$, $D_M(v_h)$ denotes the diagonal matrix with the values of $v_h \in \mathbb{R}^M$, $M \geq 1$ on the diagonal and $\mathbf{1}_M := (1, \dots, 1)^T \in \mathbb{R}^M$. Here $\mathcal{N}(\nabla_h \mathbf{u}_h) \nabla_h \mathbf{d}_{\mathbf{u}_h}$ is the discretization of the term $\nabla \mathbf{u} \cdot \nabla \mathbf{d}_{\mathbf{u}}$ in (14). Moreover, we have

$$\begin{aligned} d_{p_{h,1}} = & -p_{h,1} + D_N(m_{h,1})^{-1} \left(D_N(\alpha_1 \mathbf{1}_N) (T_h(\mathbf{u}_h + \mathbf{d}_{\mathbf{u}_h}) - g_h) \right. \\ & \left. - D_N(\chi_{h,1}) D_N(m_{h,1})^{-1} D_N(p_{h,1}) D_N(T_h \mathbf{u}_h - g_h) T_h \mathbf{d}_{\mathbf{u}_h} \right), \quad (16) \end{aligned}$$

$$\begin{aligned} \mathbf{d}_{\mathbf{p}_{h,2}} = & -\mathbf{p}_{h,2} + D_{2N}(m_{h,2})^{-1} \left(D_{2N}(\lambda \mathbf{1}_{2N}) \nabla_h(\mathbf{u}_h + \mathbf{d}_{\mathbf{u}_h}) \right. \\ & \left. - D_{2N}(\chi_{h,2}) D_{2N}(m_{h,2})^{-1} D_{2N}(\mathbf{p}_{h,2}) \mathcal{N}(\nabla_h \mathbf{u}_h) \nabla_h \mathbf{d}_{\mathbf{u}_h} \right). \quad (17) \end{aligned}$$

We note that H_h is even in the uniform case not symmetric because $\mathcal{N}(\nabla_h \mathbf{u}_h)$ is not. Indeed, if $m = 1$ (image reconstruction) for $v = (v_x, v_y) \in \mathbb{R}^{2N}$, we have

$$\mathcal{N}(v) := \begin{pmatrix} D_N(v_x) & D_N(v_y) \\ D_N(v_x) & D_N(v_y) \end{pmatrix},$$

and if $m = 2$ (optical flow estimation), for $v = (v_x^1, v_y^1, v_x^2, v_y^2) \in \mathbb{R}^{4N}$, it follows

$$\mathcal{N}(v) := \begin{pmatrix} D_N(v_x^1) & D_N(v_y^1) & D_N(v_x^2) & D_N(v_y^2) \\ D_N(v_x^1) & D_N(v_y^1) & D_N(v_x^2) & D_N(v_y^2) \\ D_N(v_x^1) & D_N(v_y^1) & D_N(v_x^2) & D_N(v_y^2) \\ D_N(v_x^1) & D_N(v_y^1) & D_N(v_x^2) & D_N(v_y^2) \end{pmatrix}.$$

In order to satisfy $|p_{h,1}| \leq \alpha_1$ and $|\mathbf{p}_{h,2}|_{F,s} \leq \lambda$, we propose to project $(p_{h,1})_i$ (resp. $(\mathbf{p}_{h,2})_i$) on the disk of radius α_1 (resp. λ) for the corresponding norms. We give in Algorithm 1 the semi-smooth Newton algorithm.

We propose to use as stopping criterion in Algorithm 1 the residual, i.e. $\|F_h(\mathbf{u}_h^n, p_{h,1}^n, \mathbf{p}_{h,2}^n)\|_{L^2(\Omega_h)} \leq \varepsilon$, for some given tolerance $\varepsilon > 0$, where F_h is the discretization of F defined in (11). Additionally, we stop the algorithm when the maximal number of iteration $\max_it \in \mathbb{N}$ is reached.

Remark. In order to guaranty the convergence of the algorithm to a minimizer of (11), we need H_h to be positive definite. Unfortunately, this is not the case in general. In order to overcome this, one could replace H_h by a positive definite matrix H_h^+ by projecting H_h into the space of positive definite matrices S_+^{2mN} , i.e. by solving

$$H_h^+ := \operatorname{argmin}_{A \in S_+^{2mN}} |A - H_h|_{F,2}.$$

Algorithm 1: Discrete semi-smooth Newton algorithm.

Data: parameters $\alpha_1, \alpha_2, \lambda, \beta, \gamma_1, \gamma_2 \geq 0$, data $g_h \in \mathbb{R}^N$, initial values $(\mathbf{u}_h^0, p_{h,1}^0, \mathbf{p}_{h,2}^0) \in \mathbb{R}^{mN} \times \mathbb{R}^N \times \mathbb{R}^{2mN}$.

Result: sequence $(\mathbf{u}_h^n, p_{h,1}^n, \mathbf{p}_{h,2}^n)_{n \in \mathbb{N}}$ approximating the solution to (10).

- 1 $n = 0$;
- 2 **while** the stopping criterion is not fulfilled **do**
- 3 Solve (15) and save the result in $\mathbf{d}_{\mathbf{u}_h}$;
- 4 Compute $d_{p_{h,1}}$ and $\mathbf{d}_{\mathbf{p}_{h,2}}$ using (16) and (17) respectively;
- 5 $\mathbf{u}_h^{n+1} = \mathbf{u}_h^n + \mathbf{d}_{\mathbf{u}_h}$;
- 6 $\mathbf{p}_{h,2}^{n+1} = \mathbf{p}_{h,2}^n + (d_{p_{h,1}}, \mathbf{d}_{\mathbf{p}_{h,2}})$;
- 7 Project $\mathbf{p}_{h,2}^{n+1}$ to satisfy $|p_{h,1}^{n+1}| \leq \alpha_1$ and $|\mathbf{p}_{h,2}^{n+1}|_{F,s} \leq \lambda$;
- 8 $n = n + 1$;
- 9 **end**

The solution of this projection has the following form [11, Section 8.1.1]

$$H_h^+ = \sum_{i=1}^{2mN} \max(0, \mu_i) \xi_i \xi_i^T, \quad (18)$$

where $(\mu_i)_i$ are the eigenvalues of the corresponding eigenvectors $(\xi_i)_i$ of H . In practice, due to the large size of the matrix H , we use sparse matrices. To compute the projection in equation (18), we need to determine all $2mN$ eigenvalues. The only available implementation for handling sparse matrices is the *implicitly restarted Arnoldi method* [34], which allows us to numerically compute at most $2mN - 1$ eigenvalues/eigenvectors. Consequently, we cannot directly use equation (18), as it requires all eigenvalues and eigenvectors. This is the reason why we use the original matrix H_h instead of H_h^+ .

8 Numerical Experiments

In this section, we solve the regularized primal problem (9) and its associated pre-dual problem (8) using the semi-smooth Newton algorithm in Algorithm 1. The energies employed here differ from those used to derive the grid refinement indicator (6). Nevertheless, a similar result as Proposition 6.1 can be shown changing the indicator (6) in the following way: for all $\mathbf{v}_h \in \mathbb{R}^{mN}$ and $(q_{h,1}, \mathbf{q}_{h,2}) \in \mathbb{R}^N \times \mathbb{R}^{2mN}$ such that $|q_{h,1}| \leq \alpha_1$ and $|\mathbf{q}_{h,2}|_{F,s} \leq \lambda$

$$\begin{aligned} h_i^{-2}(\eta_h)_i &= \alpha_1 \varphi_{\gamma_{h,1}}((T_h \mathbf{v}_h - g_h)_i) + \frac{\alpha_2}{2} (T_h \mathbf{v}_h - g_h)_i^2 + \frac{\beta}{2} \Phi_i(\mathbf{v}_h) + \lambda (|\nabla_h \mathbf{v}_h|_{F,r})_i \\ &+ \frac{1}{2} \sum_{k=1}^m (T_h^* q_{h,1} + \nabla_h^* \mathbf{q}_{h,2} - \alpha_2 T_h^* g_h)_{(k-1)N+i} (B_h^{-1} (T_h^* q_{h,1} + \nabla_h^* \mathbf{q}_{h,2} - \alpha_2 T_h^* g_h))_{(k-1)N+i} \\ &- \frac{\alpha_2}{2} (g_h)_i^2 + (g_h)_i (q_{h,1})_i + \frac{\gamma_1}{2\alpha_1} (q_{h,1})_i^2 + \frac{\gamma_2}{2\lambda} \sum_{n=1}^m \sum_{k=1}^2 (\mathbf{q}_{h,2})_{2(n-1)N+(k-1)N+i}^2, \quad (19) \end{aligned}$$

where Φ_i is defined in (7), for $i = 1, \dots, N$. Observe that, because we discard many terms in Proposition 6.1, it is possible that certain components of the indicator could turn out to be negative. More precisely, the fifth and seventh term in (19) may take on negative values, whereas the sixth term is always negative. To address this, we ensure the indicator is always positive by replacing η_h in (21) by

$$\widetilde{\eta}_h := \eta_h - \min_n (\eta_h)_n. \quad (20)$$

The initial values for the Newton algorithm are chosen to be $\mathbf{u}_h^0 = T_h^* g_h$, $p_{h,1}^0 = T_h \mathbf{u}_h^0$ and $\mathbf{p}_{h,2}^0 = \nabla_h \mathbf{u}_h^0$. Experimentally, this choice leads to a faster convergence, in terms of number of iterations, of the algorithm than setting $\mathbf{u}_h^0, p_{h,1}^0$ and $\mathbf{p}_{h,2}^0$ identically to zero. In practice, we set $B_h := \alpha_2 T_h^* T_h + \beta S_h^* S_h$ and B_h^{-1} is taken as the inverse of B_h . These choices are different from Section 3 as it is not clear that $\alpha_2 T_h^* T_h + \beta S_h^* S_h$ is the discretization of the continuous B from Section 2 and that $(\alpha_2 T_h^* T_h + \beta S_h^* S_h)^{-1}$ is the discretization of the inverse of the continuous B . In fact, the invertibility of $\alpha_2 T_h^* T_h + \beta S_h^* S_h$ remains uncertain as in the case $S_h = \nabla_h$ we do not have that $(\nabla^*)_h = (\nabla_h)^*$.

Furthermore, the semi-smooth Newton algorithm occasionally reaches the maximum allowed number of iterations, $\text{max_it} = 100$, which can result in the residual $\|F_h(\mathbf{u}_h^n, p_{h,1}^n, \mathbf{P}_{h,2}^n)\|_{L^2(\Omega_h)}$ remaining large. The implementation of the algorithms is done in the programming language Python and can be found at [28].

8.1 Application to Image Reconstruction

A grayscale image is represented by a function $f : \Omega \subseteq \mathbb{R}^2 \rightarrow [0, 1]$. Here $m = 1$ and we choose $T = Id$ and $g = f$, which leads to $T_h = Id$ and $g_h = f_h$, where f_h is the discretization of f . For the grid refinement strategy, we utilize the greedy Dörfler marking strategy [38] with $0 \leq \theta_{\text{mark}} \leq 1$, i.e. denoting by $N \in \mathbb{N}$ the number of elements of a given grid Ω_h , for given error indicators in descending order $(\tilde{\eta}_h)_n$, the algorithm refines the first $n_{\text{mark}} \in \mathbb{N}$ elements that satisfy

$$\sum_{n=1}^{n_{\text{mark}}} (\tilde{\eta}_h)_n \geq \theta_{\text{mark}} \sum_{n=1}^N (\tilde{\eta}_h)_n. \quad (21)$$

We give in Algorithm 2 the coarse-to-fine algorithm to solve the TV problem on an adaptive mesh.

Algorithm 2: Adaptive L^1 - L^2 -TV algorithm for images ($m = 1$).

Data: input image f_h of size $w \times h$, parameters $(\alpha_1, \alpha_2, \lambda, \beta, \gamma_1, \gamma_2)$, maximal number of refinement $N_{\text{ref_max}} \in \mathbb{N}$.

Result: output image \mathbf{u}_h .

- 1 Ω_h^1 uniform coarse grid of size $\lfloor \frac{w}{2^{N_{\text{ref_max}}}} \rfloor \times \lfloor \frac{h}{2^{N_{\text{ref_max}}}} \rfloor$;
 - 2 $k = 1$;
 - 3 **while** *mesh level* $< N_{\text{max_ref}}$ **do**
 - 4 compute \mathbf{u}_h using the semi-smooth Newton algorithm (Algorithm 1);
 - 5 compute the local primal-dual gap error $\tilde{\eta}_h$ using (20);
 - 6 adapt (as described in Section 3) the grid using (21) and save the resulting grid in Ω_h^{k+1} ;
 - 7 L^2 -projection of the data on the new grid Ω_h^{k+1} ;
 - 8 $k = k + 1$;
 - 9 **end**
-

8.1.1 Noiseless Case

In order to demonstrate that using the indicator $\tilde{\eta}_h$ derived from the primal-dual gap error (20) as a mesh refinement criterion may lead to a faster convergence with respect to the number of degrees of freedom (dofs) than uniform refinement we consider a simple 2D example. Let the image f be the characteristic function of the disk centered at the origin and of radius $R > 0$, i.e. $f = \mathbf{1}_{B(0,R)}$. We recall the explicit solution u_{α_1, α_2} of the problem in (\mathcal{P}) when $\Omega = \mathbb{R}^2$, $\beta = \gamma_1 = \gamma_2 = 0$ and $\alpha_1 > 0$, $\alpha_2 > 0$ found in [25]:

$$u_{\alpha_1, \alpha_2} = \begin{cases} 0, & \text{if } 0 \leq R < \frac{2}{\alpha_2 + \alpha_1}, \\ \left(\frac{\alpha_2 + \alpha_1}{\alpha_2} - \frac{2}{\alpha_2 R} \right) \mathbf{1}_{B(0,R)}, & \text{if } \frac{2}{\alpha_2 + \alpha_1} \leq R \leq \frac{2}{\alpha_1}, \\ \mathbf{1}_{B(0,R)}, & \text{if } R > \frac{2}{\alpha_1}. \end{cases}$$

In particular, if we choose $\alpha_1 = \alpha_2 = 1$ and $R = \frac{3}{2}$, we have $u_{\text{exact}} := \frac{2}{3} \mathbf{1}_{B(0,R)}$. Figure 6 shows the error between the exact solution u_{exact} and the computed discrete solution \mathbf{u}_h , i.e. $\|u_{\text{exact}} - I_h \mathbf{u}_h\|_{L^2(\Omega)}$, with respect to the number of degrees of freedom when using Algorithm 2 with a uniform mesh and an adaptive mesh on the disk. As we use the semi-smooth Newton algorithm from Section 7, we must set γ_1, γ_2 non-zero and choose $\gamma_1 = \gamma_2 = 2 \times 10^{-4}$, $\varepsilon = 1 \times 10^{-3}$ and $\theta_{\text{mark}} = 0.2$. As expected, for a given number of dofs, the adaptive algorithm gives a more accurate solution, i.e. the error is smaller, than with a uniform mesh.

In Figure 7, we show the sequence of adapted meshes corresponding to the disk example. We see that the indicator $\tilde{\eta}_h$ is well suited for mesh adaptivity since it marks elements for refinement which are located near the discontinuities (edges) of the original image.

8.1.2 Gaussian Denoising

For removing additive Gaussian noise with zero mean and standard deviation σ from an image ($m = 1$), we set $T = Id$ and we use the same algorithm as in the noiseless case, namely Algorithm 2, with the slight change that a second

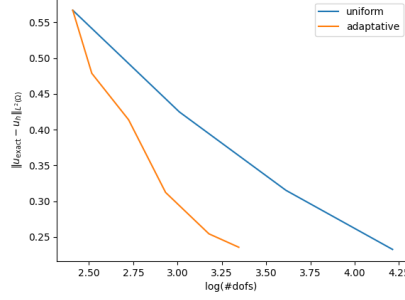


Figure 6: Convergence for the disk example.

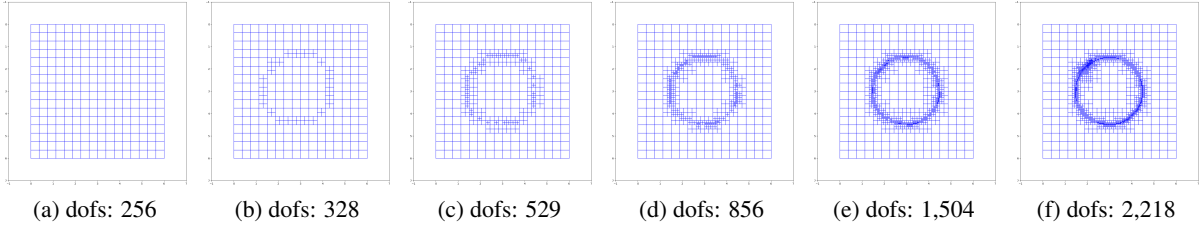


Figure 7: Adapted meshes sequence for the disk example using Algorithm 2.

condition is added to the refinement criterion named the *bulk criterion*. This approach is motivated by [26], where an element for refinement is marked when the local residual is bigger than a quantity depending on the noise level and on the size of the element by using a statistical argument in the same spirit as [20]. Here however, a different *bulk criterion* which do not depend on the size of the element is used: an element E_i with center $\mathbf{x}_i \in \Omega_h$ can be marked for refinement if

$$\frac{1}{2} h_i^2 (\mathbf{u}_h - g_h)_i^2 \geq \frac{\sigma^2}{2}. \quad (22)$$

Loosely speaking, we do an averaging of the residual on an element E_i , and if this quantity is bigger than the noise level, it means that there is an edge in the element, thus the algorithm refines E_i . This condition is similar to the one from [30]. That is here the marking strategy for refinement runs in two steps: first all elements fulfilling the bulk criterion (22) are detected and then the Dörfler marking strategy is only applied on these selected elements.

We recall the definition of the *peak signal-to-noise ratio* (PSNR) [10]

$$\text{PSNR} = 10 \log_{10} \left(\frac{1}{\frac{1}{N} \sum_{i=0}^N ((\mathbf{u}_h)_i - (g_h)_i)^2} \right).$$

The PSNR is useful to evaluate the proximity of the reconstruction to the original image. In the experiments, we will also use the *structural similarity* (SSIM). The idea of SSIM is to measure the structural similarity between two images, rather than a pixel-to-pixel difference as for example PSNR does. The measure between two windows x and y of common size $\omega \times \omega$ is [43]:

$$\text{SSIM}(x, y) = \frac{(2\mu_x \mu_y + c_1)(2\sigma_{xy} + c_2)}{(\mu_x^2 + \mu_y^2 + c_1)(\sigma_x^2 + \sigma_y^2 + c_2)},$$

where μ_x, μ_y is the pixel sample mean of x, y respectively, σ_x^2, σ_y^2 is the variance of x, y respectively, σ_{xy} is the covariance of x and y , $c_1 = 0.01^2$ and $c_2 = 0.03^2$. The constants c_1 and c_2 are chosen to stabilize the division with weak denominator. Note that when comparing PSNR and SSIM, larger values indicate a better reconstruction than smaller values.

In these experiments, we chose as model parameters $\alpha_1 = 0, \alpha_2 = 10, \lambda = 1, \beta = 0$ and $\gamma_1 = \gamma_2 = 2 \times 10^{-4}$, and we chose $N_{\max \text{ref}} = 6, \theta_{\text{mark}} = 0.6$ and $\varepsilon = 1 \times 10^{-3}$.

Table 1 shows the PSNR and the mean SSIM (MSSIM) for the denoising with both uniform and adaptive mesh for several noise level σ . We do the experiment using the *Middlebury* dataset. For image processing tasks like denoising, we aim to align the finely refined grid with the image pixels to preserve discontinuities. Therefore, we crop and resize the input image so that its width and height are powers of two (more precisely to 256×256 pixels). Otherwise, the grid

nodes may not align properly, leading to a blurred reconstruction. In every example, using a uniform mesh generates results with larger PSNR and MSSIM and less computation time than using the coarse-to-fine adaptive refinement strategy. We observe that in the coarse-to-fine approach, sometimes the PSNR increases as the noise level increases. This is because noise results in a noisy refinement indicator, and since the bulk criterion cannot differentiate edges from noise perfectly, the algorithm tends to refine the grid more uniformly, leading to more accurate reconstructions. Moreover, most of the computation time is due to the projection step of Algorithm 2, which indicate that projections might not efficiently implemented.

In Figure 8, we give from left to right, the original image from the *Middlebury* dataset, the noisy image used as input for the algorithm ($\sigma = 0.1$), the denoised image with a uniform mesh and the denoised image with an adaptive mesh. A sequence of meshes for the adaptive algorithm is given in Figure 9.

Benchmark	σ	Uniform			Adaptive		
		PSNR	MSSIM	Time (s)	PSNR	MSSIM	Time (s)
Dimetrodon	0.1	29.21	0.80	5.39	27.60	0.73	23.96
	0.05	29.59	0.80	6.07	27.69	0.75	24.05
	0.01	29.68	0.80	6.05	27.07	0.74	23.92
Grove2	0.1	25.28	0.71	7.02	23.54	0.63	23.01
	0.05	25.38	0.71	5.90	23.34	0.63	26.18
	0.01	25.39	0.71	6.36	23.26	0.62	22.98
RubberWhale	0.1	30.53	0.79	6.35	28.90	0.75	22.07
	0.05	31.26	0.80	5.75	29.71	0.78	65.20
	0.01	31.46	0.81	6.01	29.45	0.78	22.27
Urban2	0.1	29.75	0.76	6.20	28.32	0.70	23.76
	0.05	30.00	0.76	5.60	28.00	0.72	23.70
	0.01	30.06	0.76	5.61	27.88	0.71	23.74

Table 1: Quantitative results: peak signal-to-noise ratio (PSNR), structural similarity (SSIM), and computational times in seconds.

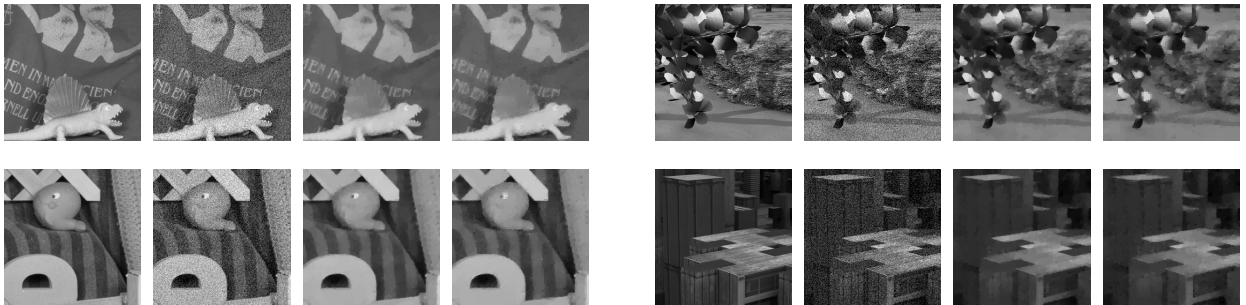


Figure 8: Middlebury Denoising Benchmark with $\sigma = 0.1$; the original image (1st and 5th column), the noisy image f with $\sigma = 0.1$ (2nd and 6th column), the denoised image using Algorithm 1 on a uniform mesh (3rd and 7th column), and the denoised image using Algorithm 2 and the bulk criterion (22) (4th and 8th column). Benchmarks from top-left to bottom-right: *Dimetrodon*, *Grove2*, *RubberWhale*, *Urban2*.

8.2 Application to Optical Flow Computation

The estimation of optical flow consists in finding a vector field $\mathbf{u} = (u_x, u_y)$, called the optical flow, describing the motion of each pixel between two frames $f_0, f_1 : \Omega \subset \mathbb{R}^2 \rightarrow [0, 1]$ of a given sequence. To this end, it is classical to consider the so-called *brightness constancy assumption* which assumes that the intensity of pixels remains constant along their trajectories. More precisely, for $\mathbf{x} \in \Omega$, we assume that

$$f_0(\mathbf{x}) = f_1(\mathbf{x} + \mathbf{u}(\mathbf{x})). \quad (23)$$

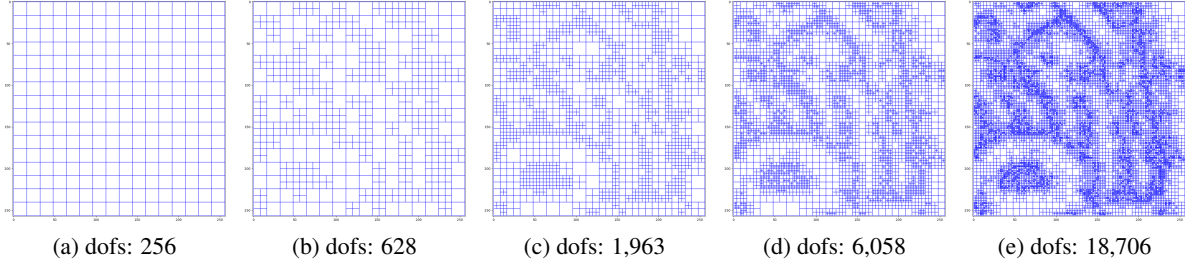


Figure 9: Adapted meshes sequence for Algorithm 2 with the *bulk criterion* (22) on the *RubberWhale* example ($\sigma = 0.05$).

Exceeding displacements $\mathbf{x} + \mathbf{u}(\mathbf{x}) \notin \Omega$ are ignored. We use the L^1 - L^2 -TV model to estimate the optical flow by setting

$$T = (\partial_x f_1 \quad \partial_y f_1), \quad S = \nabla, \quad \text{and} \quad g := T\mathbf{u}_0 - (f_1 - f_0),$$

which leads to

$$T_h = (\partial_x^c f_1 \quad \partial_y^c f_1), \quad S_h = \nabla_h, \quad \text{and} \quad g_h = T_h \mathbf{u}_{h,0} - (f_{h,1} - f_{h,0}),$$

with \mathbf{u}_0 a given initial guess of the optical flow and $\mathbf{u}_{h,0}$ its discretization, and $f_{h,0}, f_{h,1}$ the discretization of f_0 and f_1 . We recall in Algorithm 3, the optical flow estimation algorithm using warping [23, Algorithm 3]. The warping technique consists in replacing f_1 by a *warped* image $f_w(\mathbf{x}) := f_1(\mathbf{x} + \mathbf{u}_0(\mathbf{x}))$, introduced after the linearization of the optical flow equation (23). The linearized optical flow equation provides flow information only in the image gradient direction, a phenomenon also known as *aperture problem*. The optical flow estimation algorithm with warping reads:

Algorithm 3: Optical flow algorithm with warping [23, Algorithm 3].

Data: images $f_{h,0}, f_{h,1}$, initial optical flow guess $\mathbf{u}_{h,0}$.

Result: motion fields $(\mathbf{u}_{h,k})_{k \in \mathbb{N}}$.

- 1 Ω_h is a uniform grid where the degrees of freedom are located in the center of the pixels;
 - 2 $f_{w,0}(\mathbf{x}) = f_{h,1}(\mathbf{x} + \mathbf{u}_{h,0}(\mathbf{x}))$;
 - 3 $k = 0$;
 - 4 **while** the stopping criterion is not fulfilled **do**
 - 5 compute $\mathbf{u}_{h,k}$ using the semi-smooth Newton algorithm (Algorithm 1) on Ω_h ;
 - 6 $f_{w,k}(\mathbf{x}) = f_{h,1}(\mathbf{x} + \mathbf{u}_{h,k}(\mathbf{x}))$;
 - 7 $k = k + 1$;
 - 8 **end**
-

Here, the line $f_{w,k}(\mathbf{x}) = f_{h,1}(\mathbf{x} + \mathbf{u}_{h,k}(\mathbf{x}))$ is to be understood as a bilinear interpolation on the finest uniform grid. We use in Algorithm 3 the stopping criterion

$$\frac{\|f_{w,k-1} - f_{h,0}\|_{L^2(\Omega_h)} - \|f_{w,k} - f_{h,0}\|_{L^2(\Omega_h)}}{\|f_{w,k-1} - f_{h,0}\|_{L^2(\Omega_h)}} \leq \varepsilon_{\text{warp}},$$

for some specified constant $\varepsilon_{\text{warp}}$, which ensures that warping continues only as long as the remaining image difference $\|f_{w,k} - f_{h,0}\|_{L^2(\Omega_h)}$ is being reduced sufficiently. Now, we recall in Algorithm 4 the optical flow estimation algorithm with adaptive warping [2, Algorithm 1]:

Unlike the image reconstruction case, we choose to refine 75% of the degree of freedom with the highest error η_h instead of using the Dörfler marking strategy. In practice, for optical flow, the primal-dual gap error is significant at a few elements, indicating that only a small portion of elements contribute to the overall error. Consequently, the Dörfler strategy results in an excessively sparse grid, leading to inaccurate optical flow estimation.

We recall the definition of the endpoint error [5]

$$\text{EE} = \sqrt{(u_x - u_{\text{GT},x})^2 + (u_y - u_{\text{GT},y})^2},$$

Algorithm 4: Optical flow algorithm with adaptive warping [2, Algorithm 1].

Data: images $f_{h,0}, f_{h,1}$ of size $w \times h$, initial optical flow guess $\mathbf{u}_{h,0}$, maximal number of refinement $N_{\text{ref_max}} \in \mathbb{N}$.

Result: motion fields $(\mathbf{u}_{h,k})_{k \in \mathbb{N}}$.

- 1 $f_{w,0}(\mathbf{x}) = f_1(\mathbf{x} + \mathbf{u}_{h,0}(\mathbf{x}))$;
- 2 Ω_h^1 uniform coarse grid of size $\lfloor \frac{w}{2^{N_{\text{ref_max}}}} \rfloor \times \lfloor \frac{h}{2^{N_{\text{ref_max}}}} \rfloor$;
- 3 $k = 1$;
- 4 $N_{\text{ref}} = 0$;
- 5 **while** $N_{\text{ref}} < N_{\text{ref_max}}$ **do**
- 6 compute $\mathbf{u}_{h,k}$ using the semi-smooth Newton algorithm (Algorithm 1) on the mesh Ω_h^k ;
- 7 $f_{w,k}(\mathbf{x}) = f_{h,1}(\mathbf{x} + \mathbf{u}_{h,k}(\mathbf{x}))$;
- 8 **if** $\frac{\|f_{w,k-1} - f_{h,0}\|_{L^2(\Omega_h)} - \|f_{w,k} - f_{h,0}\|_{L^2(\Omega_h)}}{\|f_{w,k-1} - f_{h,0}\|_{L^2(\Omega_h)}} \leq \varepsilon_{\text{warp}}$ **then**
- 9 refine the grid Ω_h^k , save it in Ω_h^{k+1} and reproject image data (L^2 -projection);
- 10 $N_{\text{ref}} = N_{\text{ref}} + 1$;
- 11 **end**
- 12 $k = k + 1$;
- 13 **end**

where $\mathbf{u} = (u_x, u_y)$ is an approximation of the optical flow and $\mathbf{u}_{\text{GT}} = (u_{\text{GT},x}, u_{\text{GT},y})$ is the *ground-truth* optical flow and the definition of the angular error [5]

$$\text{AE} = \arccos \frac{1 + u_x u_{\text{GT},x} + u_y u_{\text{GT},y}}{\sqrt{1 + u_x^2 + u_y^2} \sqrt{1 + u_{\text{GT},x}^2 + u_{\text{GT},y}^2}}.$$

These two errors are the most commonly used measures of performance for optical flow. The AE between a flow vector $\mathbf{u} = (u_x, u_y)$ and the ground-truth flow $\mathbf{u}_{\text{GT}} = (u_{\text{GT},x}, u_{\text{GT},y})$ is the angle between the estimated optical flow vectors and the *ground-truth* vectors, while the EE quantify the Euclidean norm of the difference between the estimated optical flow vectors and the *ground-truth* vectors.

In our optical flow experiments, we set $\alpha_1 = 3$, $\alpha_2 = 0$, $\lambda = 1$, $\beta = 1 \times 10^{-5}$ and $\gamma_1 = \gamma_2 = 2 \times 10^{-4}$ and as initial optical flow guess $\mathbf{u}_{h,0} = 0$. For Algorithm 3 and Algorithm 4, we chose $\varepsilon_{\text{warp}} = 5 \times 10^{-2}$ and for Algorithm 1, we chose $\varepsilon = 1 \times 10^{-3}$.

In Table 2, we give endpoint errors (EE) and angular errors (AE), each given by mean and standard deviation, and computational times in seconds for the *Middlebury* dataset where the *ground-truth* optical flows are known for the computed optical flow \mathbf{u} without warping (first iteration of Algorithm 3), with warping (Algorithm 3) and the computed optical flow \mathbf{u} using the adaptive warping (Algorithm 4). The *ground-truth* optical flow is the exact optical flow between the image $f_{h,0}$ and $f_{h,1}$. Unlike denoising, it is uncertain whether the discontinuities in optical flow align with those in the images. Therefore, there is no need to adjust the size of the input images, as the alignment of discontinuities is not as critical for optical flow estimation.

For the examples *Dimetrodon*, *Grove3*, *Hydrangea*, *RubberWhale* and *Venus* the uniform grid with warping, i.e. Algorithm 3, gives the lowest endpoint and angular errors. However, this accuracy has a price in terms of number of degrees of freedom (dofs), and as a result, of computation time. On the other hand, the results without warping give the highest errors in all the examples due to the linearization of the optical flow estimation problem. Finally, the adaptive warping, Algorithm 4, gives similar results as for the uniform warping, but with a computation cost similar as for the non-warping case. For *Grove2*, *Urban2* and *Urban3*, we notice that the errors with adaptive warping are even smaller than uniform warping.

We give in Figure 10 the images from the *Middlebury* dataset f_0, f_1 , the image difference $f_0 - f_1$, the computed optical flow using without warping (first iteration of Algorithm 3) and with warping (Algorithm 3), the computed optical flow using the adaptive warping (Algorithm 4) and the *ground-truth* optical flow. The color-coded images representing optical flow fields are normalized by the maximum motion of the *ground-truth* flow data and black areas of the ground truth data represent unknown flow information, e.g. due to occlusion.

Figure 11 depicts a sequence of adapted meshes with the criterion (20). The mesh seems to be finer near the edges of the *ground-truth*, which is where the movement is concentrated.

Note that the results are similar to the ones in [2], where the adaptive finite element method have been used to solve the semi-smooth Newton iterations.

Benchmark	Algorithm	EE-mean	EE-stddev	AE-mean	AE-stddev	Time (s)
Dimetrodon	Uniform without warping	1.47	0.74	0.63	0.36	429.44
	Uniform with warping	0.26	0.25	0.19	0.49	2,598.29
	Adaptive warping, Algorithm 4	0.42	0.37	0.23	0.48	1,066.91
Grove2	Uniform without warping	2.79	0.47	0.98	0.18	726.93
	Uniform with warping	1.09	1.16	0.35	0.42	9,211.81
	Adaptive warping, Algorithm 4	0.38	0.62	0.10	0.18	1,686.60
Grove3	Uniform without warping	3.51	2.35	0.86	0.34	723.02
	Uniform with warping	1.22	1.75	1.18	0.30	13,010.78
	Adaptive warping, Algorithm 4	1.32	1.67	0.22	0.36	1,823.77
Hydrangea	Uniform without warping	3.10	1.20	0.78	0.29	349.94
	Uniform with warping	0.25	0.53	0.14	0.41	6,830.48
	Adaptive warping, Algorithm 4	0.45	0.69	0.18	0.43	1,307.07
RubberWhale	Uniform without warping	0.54	0.60	0.30	0.32	424.89
	Uniform with warping	0.29	0.54	0.17	0.34	1,799.16
	Adaptive warping, Algorithm 4	0.47	0.61	0.29	0.38	1,257.92
Urban2	Uniform without warping	7.95	8.12	0.82	0.42	793.44
	Uniform with warping	6.19	7.70	0.27	0.32	10,212.01
	Adaptive warping, Algorithm 4	1.52	2.30	0.17	0.31	1,493.25
Urban3	Uniform without warping	6.89	4.45	1.02	0.29	2,401.56
	Uniform with warping	4.86	4.11	0.49	0.62	11,855.79
	Adaptive warping, Algorithm 4	2.38	3.59	0.39	0.79	1,401.86
Venus	Uniform without warping	3.32	1.72	0.82	0.26	273.16
	Uniform with warping	0.70	1.01	0.19	0.44	4,514.02
	Adaptive warping, Algorithm 4	1.16	1.33	0.32	0.59	744.36

Table 2: Quantitative results: endpoint errors (EE) and angular errors (AE), each given by mean and standard deviation, and computational times in seconds.

9 Conclusion

We introduced a novel adaptive finite difference scheme to solve the L^1 - L^2 -TV problem numerically, leading to a non-uniform discretization of the image domain. From our numerical experiments we conclude that an adaptive meshing in a finite difference setting can be beneficial. In particular the degrees of freedom can be significantly reduced. In the task of estimating the optical flow we could additionally observe that our coarse-to-fine scheme reduces computation time and sometimes even improves the quality of the result as well, promoting our approach.

While adaptively changing the underlying mesh can be advantageous in a computational setting, we also investigated the influence of a refinement on the discrete total variation. It turns out that the discrete total variation is indeed dependent on the grid. In particular, a refinement may increase, but does not decrease, the total variation of a function, cf. Section 5. While this property is plausible and obviously has an effect on the minimization of the total variation, it is not clear to us if and how it influences the Γ -convergence of the discrete total variation to the continuous one.

References

- [1] C. D. Aliprantis and K. C. Border. *Infinite Dimensional Analysis*. Springer-Verlag, Berlin/Heidelberg, 2006.
- [2] M. Alkämper, S. Hilb, and A. Langer. A primal-dual adaptive finite element method for total variation based motion estimation, 2024. ArXiv:2404.03125.

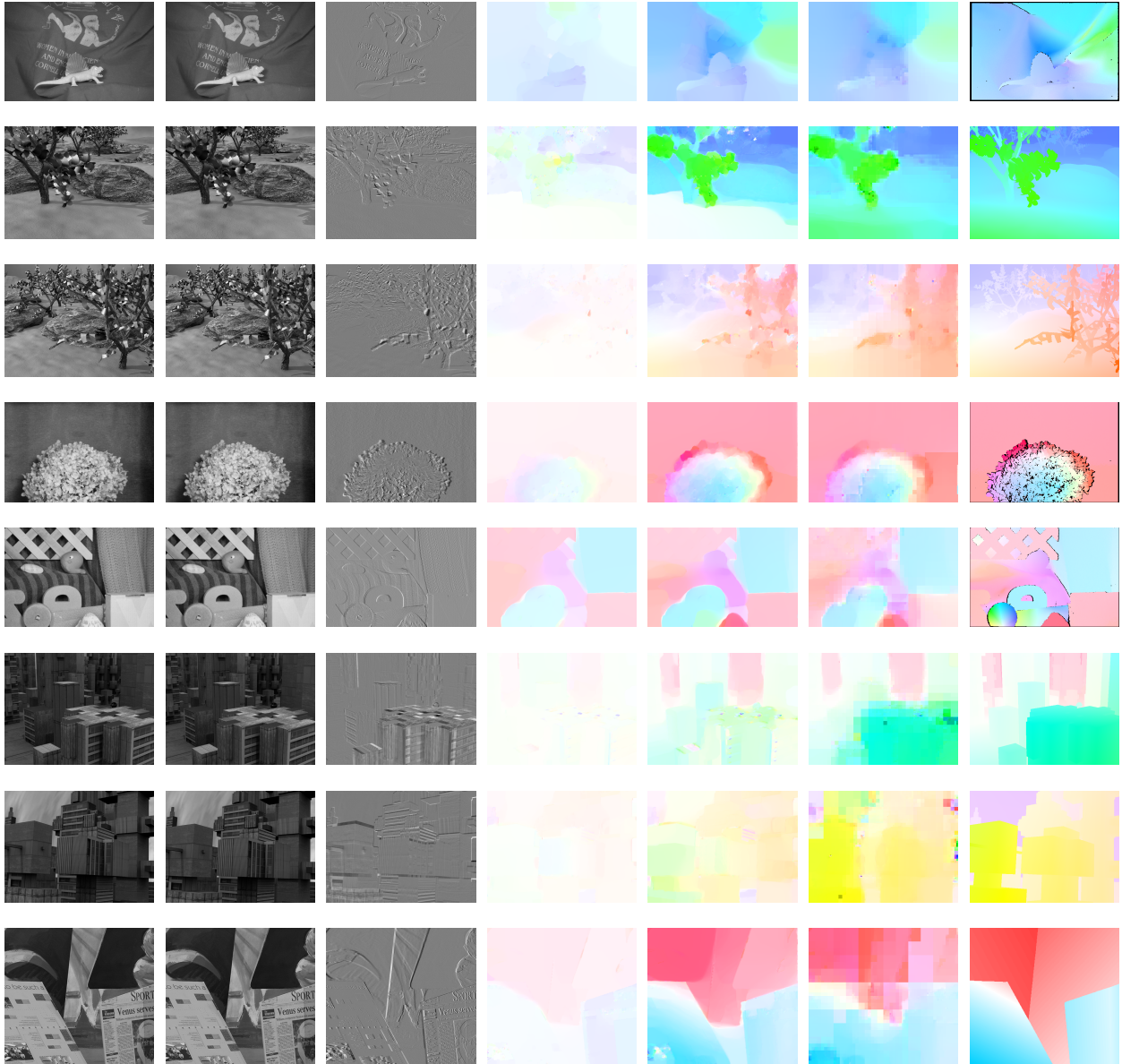


Figure 10: Middlebury Optical Flow Benchmark; columns from left to right: f_0 , f_1 , image difference $f_0 - f_1$, computed optical flow \mathbf{u} using without warping and with warping, computed optical flow \mathbf{u} using Algorithm 4 (adaptive warping), ground truth optical flow. Benchmarks from top to bottom: *Dimetrodon*, *Grove2*, *Grove3*, *Hydrangea*, *RubberWhale*, *Urban2*, *Urban3*, *Venus*.

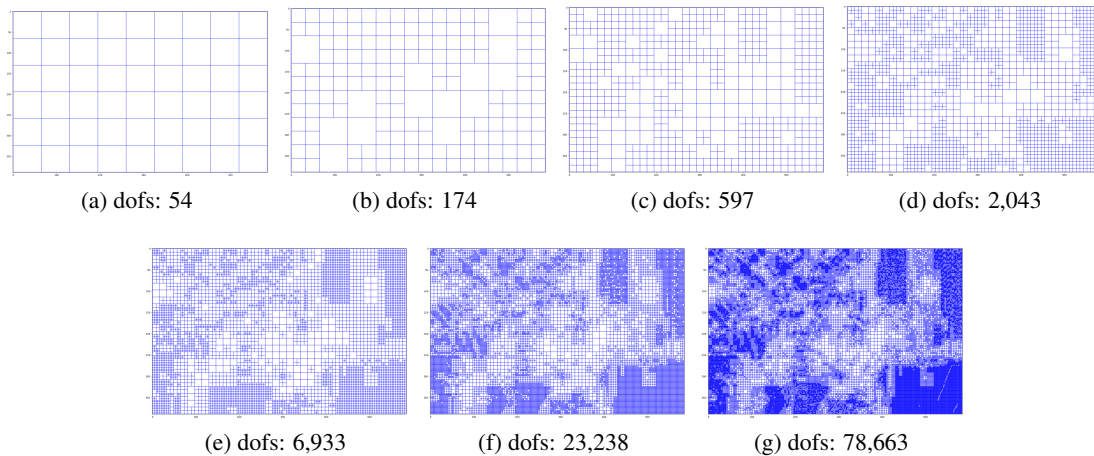


Figure 11: Adapted meshes sequence for Algorithm 4 on the *RubberWhale* example.

- [3] M. Alkämper and A. Langer. Using DUNE-ACFem for non-smooth minimization of bounded variation functions. *Archive of Numerical Software*, Vol 5:3–19 Pages, 2017.
- [4] S. Alliney. A property of the minimum vectors of a regularizing functional defined by means of the absolute norm. *IEEE Transactions on Signal Processing*, 45(4):913–917, 1997.
- [5] S. Baker, S. Roth, D. Scharstein, M. J. Black, J. Lewis, and R. Szeliski. A database and evaluation methodology for optical flow. In *2007 IEEE 11th International Conference on Computer Vision*, pages 1–8, 2007. ISSN: 2380-7504.
- [6] S. Bartels. Total variation minimization with finite elements: Convergence and iterative solution. *SIAM Journal on Numerical Analysis*, 50(3):1162–1180, 2012.
- [7] S. Bartels and A. Kaltenbach. Explicit a posteriori error representation for variational problems and application to TV-minimization, 2023. arXiv:2307.04022.
- [8] S. Bartels and M. Milicevic. Primal-dual gap estimators for a posteriori error analysis of nonsmooth minimization problems. *ESAIM: Mathematical Modelling and Numerical Analysis*, 54(5):1635–1660, 2020.
- [9] M. J. Berger and P. Colella. Local adaptive mesh refinement for shock hydrodynamics. *Journal of Computational Physics*, 82(1):64–84, 1989.
- [10] A. C. Bovik. *Handbook of Image and Video Processing*. Academic Press Series in Communications, Networking, and Multimedia. Academic Press, San Diego San Francisco New York [etc.], 2000.
- [11] S. Boyd and L. Vandenberghe. *Convex Optimization*. Cambridge University Press, 1 edition, 2004.
- [12] A. Buades, B. Coll, and J. M. Morel. A review of image denoising algorithms, with a new one. *Multiscale Modeling & Simulation*, 4(2):490–530, 2005.
- [13] C. Caillaud and A. Chambolle. Error estimates for finite differences approximations of the total variation. *IMA Journal of Numerical Analysis*, 43(2):692–736, 2023.
- [14] A. Chambolle. An algorithm for total variation minimization and applications. *Journal of Mathematical Imaging and Vision*, 20(1):89–97, 2004.
- [15] A. Chambolle, V. Caselles, D. Cremers, M. Novaga, and T. Pock. An introduction to total variation for image analysis. In M. Fornasier, editor, *Theoretical Foundations and Numerical Methods for Sparse Recovery*, pages 263–340. De Gruyter, 2010.
- [16] A. Chambolle and P.-L. Lions. Image recovery via total variation minimization and related problems. *Numerische Mathematik*, 76(2):167–188, 1997.
- [17] A. Chambolle and T. Pock. Approximating the total variation with finite differences or finite elements. In *Handbook of Numerical Analysis*, volume 22, pages 383–417. Elsevier, 2021.
- [18] L. Condat. Discrete total variation: New definition and minimization. *SIAM Journal on Imaging Sciences*, 10(3):1258–1290, 2017.

- [19] M. de Berg, M. van Krefeld, M. Overmars, and O. Cheong. *Computational Geometry: Algorithms and Applications*. Springer Berlin Heidelberg, Berlin, Heidelberg, 2nd ed. 2000 edition, 2000. OCLC: 1227482129.
- [20] Y. Dong, M. Hintermüller, and M. M. Rincon-Camacho. Automated regularization parameter selection in multi-scale total variation models for image restoration. *Journal of Mathematical Imaging and Vision*, 40(1):82–104, 2011.
- [21] I. Ekeland and R. Témam. *Convex Analysis and Variational Problems*. Society for Industrial and Applied Mathematics, 1999.
- [22] S. Hilb. *Total Variation Minimization via Dual-Based Methods and its Discretization Aspects*. PhD thesis, University of Stuttgart, Stuttgart, 2023.
- [23] S. Hilb, A. Langer, and M. Alkämper. A primal-dual finite element method for scalar and vectorial total variation minimization. *Journal of Scientific Computing*, 96(1):24, 2023.
- [24] M. Hintermüller, A. Langer, C. N. Rautenberg, and T. Wu. Adaptive regularization for image reconstruction from subsampled data. In X.-C. Tai, E. Bae, and M. Lysaker, editors, *Imaging, Vision and Learning Based on Optimization and PDEs*, pages 3–26, Cham, 2018. Springer International Publishing.
- [25] M. Hintermüller and A. Langer. Subspace correction methods for a class of nonsmooth and nonadditive convex variational problems with mixed L^1/L^2 data-fidelity in image processing. *SIAM Journal on Imaging Sciences*, 6(4):2134–2173, 2013.
- [26] M. Hintermüller and M. Rincon-Camacho. An adaptive finite element method in L^2 -TV-based image denoising. *Inverse Problems & Imaging*, 8(3):685–711, 2014.
- [27] M. Hintermüller and G. Stadler. An infeasible primal-dual algorithm for total bounded variation–based inf-convolution-type image restoration. *SIAM Journal on Scientific Computing*, 28(1):1–23, 2006.
- [28] T. Jacumin. thomasjacumin/adaptive-11-l2-tv: Second release.
- [29] A. Langer. *Subspace Correction and Domain Decomposition Methods for Total Variation Minimization*. PhD thesis, Johannes Kepler Universität, Linz, 2011.
- [30] A. Langer. Automated parameter selection for total variation minimization in image restoration. *Journal of Mathematical Imaging and Vision*, 57(2):239–268, 2017.
- [31] A. Langer. Automated parameter selection in the L^1 - L^2 -TV model for removing Gaussian plus impulse noise. *Inverse Problems*, 33(7):074002, 2017.
- [32] A. Langer. Locally adaptive total variation for removing mixed Gaussian–impulse noise. *International Journal of Computer Mathematics*, 96(2):298–316, 2019.
- [33] A. Langer and S. Behnamian. DeepTV: A neural network approach for total variation minimization, 2024. arXiv:2409.05569.
- [34] R. B. Lehoucq, D. C. Sorensen, and C. Yang. *ARPACK Users’ Guide: Solution of Large-Scale Eigenvalue Problems with Implicitly Restarted Arnoldi Methods*. Society for Industrial and Applied Mathematics, 1998.
- [35] C. Min, F. Gibou, and H. D. Ceniceros. A supra-convergent finite difference scheme for the variable coefficient Poisson equation on non-graded grids. *Journal of Computational Physics*, 218(1):123–140, 2006.
- [36] M. Nikolova. Minimizers of cost-functions involving nonsmooth data-fidelity terms. Application to the processing of outliers. *SIAM Journal on Numerical Analysis*, 40(3):965–994 (electronic), 2002.
- [37] M. Nikolova. A variational approach to remove outliers and impulse noise. *Journal of Mathematical Imaging and Vision*, 20(1-2):99–120, 2004.
- [38] R. H. Nochetto, K. G. Siebert, and A. Veiser. Theory of adaptive finite element methods: An introduction. In R. DeVore and A. Kunoth, editors, *Multiscale, Nonlinear and Adaptive Approximation*, pages 409–542, Berlin, Heidelberg, 2009. Springer Berlin Heidelberg.
- [39] A. M. Oberman and I. Zwiers. Adaptive finite difference methods for nonlinear elliptic and parabolic partial differential equations with free boundaries. *Journal of Scientific Computing*, 68(1):231–251, 2016.
- [40] L. I. Rudin, S. Osher, and E. Fatemi. Nonlinear total variation based noise removal algorithms. *Physica D: Nonlinear Phenomena*, 60(1):259–268, 1992.
- [41] J. Shen and T. F. Chan. Mathematical models for local nontexture inpaintings. *SIAM Journal on Applied Mathematics*, 62(3):1019–1043, 2002.
- [42] J. Wang and B. J. Lucier. Error bounds for finite-difference methods for Rudin–Osher–Fatemi image smoothing. *SIAM Journal on Numerical Analysis*, 49(2):845–868, 2011.

- [43] Z. Wang, E. Simoncelli, and A. Bovik. Multiscale structural similarity for image quality assessment. In *The Thirty-Seventh Asilomar Conference on Signals, Systems & Computers*, pages 1398–1402, Pacific Grove, CA, USA, 2003. IEEE.
- [44] C. Zach, T. Pock, and H. Bischof. A duality based approach for realtime TV- L^2 optical flow. In F. A. Hamprecht, C. Schnörr, and B. Jähne, editors, *Pattern Recognition*, volume 4713, pages 214–223. Springer Berlin Heidelberg, Berlin, Heidelberg, 2007. Series Title: Lecture Notes in Computer Science.

A Proof of the Primal-Dual Gap Error Estimation

The energy E satisfies the following property (see for example [22, Lemma 3.7]):

Lemma A.1. *If \mathbf{u} is a minimizer of (\mathcal{P}) , then we have*

$$\frac{1}{2} \|\mathbf{v} - \mathbf{u}\|_B^2 \leq E(\mathbf{v}) - E(\mathbf{u}),$$

for all \mathbf{v} in $H^1(\Omega)^m$.

Now we give the proof of Proposition 6.1.

Proof of Proposition 6.1. We recall that I_h denotes the piecewise constant interpolation. By Lemma A.1 we have,

$$\frac{1}{2} \|I_h \mathbf{u}_h - \mathbf{u}\|_B^2 \leq E(I_h \mathbf{u}_h) - E(\mathbf{u}).$$

The strong duality of the continuous problems leads to,

$$\begin{aligned} \frac{1}{2} \|I_h \mathbf{u}_h - \mathbf{u}\|_B^2 &\leq E(I_h \mathbf{u}_h) - D(p_1, \mathbf{p}_2) \leq E(I_h \mathbf{u}_h) - D(I_h p_{h,1}, I_h \mathbf{p}_{h,2}) \\ &= \eta_h(\mathbf{u}_h, p_{h,1}, \mathbf{p}_{h,2}) + (E(I_h \mathbf{u}_h) - E_h(\mathbf{u}_h)) - (D(I_h p_{h,1}, I_h \mathbf{p}_{h,2}) - D_h(p_{h,1}, \mathbf{p}_{h,2})) \\ &\leq \eta_h(\mathbf{v}_h, q_{h,1}, \mathbf{q}_{h,2}) + (E(I_h \mathbf{u}_h) - E_h(\mathbf{u}_h)) + (D_h(p_{h,1}, \mathbf{p}_{h,2}) - D(I_h p_{h,1}, I_h \mathbf{p}_{h,2})). \end{aligned}$$

The last term in the above inequality can be written as

$$\begin{aligned} D_h(p_{h,1}, \mathbf{p}_{h,2}) - D(I_h p_{h,1}, I_h \mathbf{p}_{h,2}) &= \frac{\alpha_2}{2} \left(\|g_h\|_{L^2(\Omega_h)}^2 - \|g\|_{L^2(\Omega)}^2 \right) + \left(\langle g, I_h p_{h,1} \rangle_{L^2(\Omega)} - \langle g_h, p_{h,1} \rangle_{L^2(\Omega_h)} \right) \\ &\quad + \frac{1}{2} \left(\|T^* I_h p_{h,1} + \nabla^* I_h \mathbf{p}_{h,2} + \alpha_2 T^* g\|_{B^{-1}}^2 - \|T_h^* q_{h,1} + \nabla_h^* \mathbf{q}_{h,2} - \alpha_2 T_h^* g_h\|_{B_h^{-1}}^2 \right). \end{aligned} \quad (24)$$

The first term can be bounded from above as follows

$$\begin{aligned} \|g_h\|_{L^2(\Omega_h)}^2 - \|g\|_{L^2(\Omega)}^2 &= \sum_{i=1}^N h_i^2 (I_h g_h)(x_i)^2 - \|g\|_{L^2(\Omega)}^2 = \sum_{i=1}^N \int_{E_i} (I_h g_h)(x_i)^2 dx - \|g\|_{L^2(\Omega)}^2 \\ &= \sum_{i=1}^N \int_{E_i} (I_h g_h)^2 dx - \|g\|_{L^2(\Omega)}^2 = \|I_h g_h\|_{L^2(\Omega)}^2 - \|g\|_{L^2(\Omega)}^2 \\ &\leq \|g - I_h g_h\|_{L^2(\Omega)} \|g + I_h g_h\|_{L^2(\Omega)}. \end{aligned}$$

Since by definition, $I_h g_h$ is the L^2 -projection of g into the space of piecewise constant functions, it follows using [1, Lemma 6.54] that $\|I_h g_h\|_{L^2(\Omega)} \leq \|g\|_{L^2(\Omega)}$ and thus

$$\|g_h\|_{L^2(\Omega_h)}^2 - \|g\|_{L^2(\Omega)}^2 \leq 2\|g\|_{L^2(\Omega)} \|g - I_h g_h\|_{L^2(\Omega)}.$$

For the second term in (24), we have

$$\begin{aligned} \langle g, I_h p_{h,1} \rangle_{L^2(\Omega)} - \langle g_h, p_{h,1} \rangle_{L^2(\Omega_h)} &= \langle g, I_h p_{h,1} \rangle_{L^2(\Omega)} - \langle I_h g_h, I_h p_{h,1} \rangle_{L^2(\Omega)} = \langle g - I_h g_h, I_h p_{h,1} \rangle_{L^2(\Omega)} \\ &\leq \|I_h p_{h,1}\|_{L^2(\Omega)} \|g - I_h g_h\|_{L^2(\Omega)} \leq \alpha_1 |\Omega| \|g - I_h g_h\|_{L^2(\Omega)}. \end{aligned}$$

So that

$$D_h(p_{h,1}, \mathbf{p}_{h,2}) - D(I_h p_{h,1}, I_h \mathbf{p}_{h,2}) \leq c \|g - I_h g_h\|_{L^2(\Omega)} + Q_h(p_{h,1}, \mathbf{p}_{h,2})$$

with $c \geq 0$, where

$$Q_h(p_{h,1}, \mathbf{p}_{h,2}) := \frac{1}{2} \left(\|T^* I_h p_{h,1} + \nabla^* I_h \mathbf{p}_{h,2} + \alpha_2 T^* g\|_{B^{-1}}^2 - \|T_h^* q_{h,1} + \nabla_h^* \mathbf{q}_{h,2} - \alpha_2 T_h^* g_h\|_{B_h^{-1}}^2 \right).$$

□